Universidade de Aveiro Departamento de Física
2009

Luís Filipe Martins Leite Ferreira

MONITORIZAÇÃO DA TOPOGRAFIA DE UMA PRAIA COM SENSORES EM FIBRA ÓPTICA

MONITORIZATION OF BED LEVEL CHANGES USING OPTICAL FIBER SENSORS

Universidade de Aveiro Departamento de Física
2009

Luís Filipe Martins Leite Ferreira

MONITORIZAÇÃO DA TOPOGRAFIA DE UMA PRAIA COM SENSORES EM FIBRA ÓPTICA

MONITORIZATION OF BED LEVEL CHANGES USING OPTICAL FIBER SENSORS

dissertação apresentada à Universidade de Aveiro para cumprimento dos requisitos necessários à obtenção do grau de Mestre em Engenharia Física, realizada sob a orientação científica do Dr. Paulo Sérgio Brito André, Professor Auxiliar Convidado do Departamento de Física da Universidade de Aveiro e do Dr. Paulo Manuel Cruz Alves da Silva, Professor Auxiliar do Departamento de Física da Universidade de Aveiro

o júri

presidente	Doutor João de Lemos Pinto Professor Catedrático do Departamento de Física da Universidade de Aveiro
vogal - arguente principal	Doutor Manuel Joaquim Bastos Marques Professor Auxiliar da Faculdade de Ciências da Universidade do Porto
vogal - orientador	Doutor Paulo Sérgio de Brito André Investigador Auxiliar no Instituto de Telecomunicações e Professor Auxiliar Convidado do Departamento de Física da Universidade de Aveiro
vogal - co-orientador	Doutor Paulo Manuel Cruz Alves da Silva Professor Auxiliar do Departamento de Física da Universidade de Aveiro

agradecimentos

Esta tese não se resume apenas a um culminar de horas de pesquisa, estudo, trabalho e reflexão. Foi através da sua realização que consegui obter um conhecimento mais aprofundado acerca das áreas abordadas, assim como um grande crescimento pessoal e acima de tudo académico. Tudo isto não seria possível sem o apoio incondicional de algumas pessoas, às quais devo os meus mais sinceros agradecimentos e que me permitiram atingir o objectivo a que me propus.

Deste modo, e em primeiro lugar, quero agradecer ao Professor Paulo Sérgio Brito André e ao Professor Paulo Manuel Cruz Alves da Silva pela disponibilidade demonstrada, incansáveis sugestões, empenho, e motivação dadas ao longo de todo o tempo, principalmente quando estive mais desanimado.

Quero também agradecer à Universidade de Aveiro, em especial ao Departamento de Física e ao Laboratório de Óptica, pelos vastos recursos humanos e materiais disponíveis, que facilitaram e me auxiliaram na realização desta tese.

Aos meus colegas do Laboratório de Óptica, em especial ao Paulo Antunes, à Fátima Domingues e à Lúcia Bilro, por todo os conselhos e apoio prestado no decurso desta tese.
Ao Tiago Abreu e ao Hervé Michallet, pelas importantes ideias, noções e sugestões na área de processos costeiros.
Agradeço também à Fundação para a Ciência e Tecnologia, por me ter concedido uma bolsa de Investigação no âmbito do projecto BRISA.

Por fim, mas não menos importante, um sentido agradecimento aos meus pais e irmãs, pelo apoio emocional, constante incentivo, e sábios conselhos da vida que nos fazem crescer e querer ir sempre mais além do aquilo que julgamos possível.

Um agradecimento muito especial ao Pedro e ao Licínio, pela amizade, apoio constante, paciência e compreensão ao longo deste ano findo.

A todos, o meu muito obrigado.

Luís

Este trabalho foi desenvolvido no âmbito do projecto

"BRISA: Interacção entre a rebentação das ondas e o transporte de areias"

PTDC/ECM/67411/2006

,
.

keywords

Optical fiber, sensor, fiber Bragg grating, beach hydromorphodynamics, swash zone, bathymetry, topography.

abstract

Fiber Bragg grating (FBG) based sensors have many advantages over conventional electric and alternative fiber optic sensor configurations. These features and their inherent compatibility with fiber-reinforced composite materials permit in-fiber gratings to be applied in several applications and in distinct environments. An optical fiber Bragg grating sensor was developed, with the capability of monitoring remotely and in real-time the bed level changes in nearshore regions through the height measurement of the sediment column above it.

An early version of the sensor was tested in a field campaign where were collected some important data in the wave breaking and swash zones. This data was processed and analyzed aiming the comprehension of hydrodynamics of that specific region, as well as estimate the sediment transport and the bathymetry/topography profile changes, comparing it with other measurements obtained by different methods. Characterization of typical cross-shore velocities in a time series for wave breaking and swash zone was also achieved.

palavras-chave

Fibra óptica, sensor, rede de Bragg, hidromorfodinâmica costeira, zona de swash, batimetria, topografia.

resumo

Sensores baseados em redes de Bragg em fibra óptica apresentam inúmeras vantagens face aos sensores electrónicos convencionais ou mesmo face a outros sensores ópticos. Estas características, bem como a sua compatibilidade com diversos tipos de materiais, permitem que os dispositivos baseados nesta tecnologia possam ser aplicados em diversas aplicações e em ambientes muito distintos. Neste trabalho, é feita a descrição do desenvolvimento de um sensor capaz de monitorizar, remotamente e em tempo real, as variações da topografia de uma praia através de medidas de altura da coluna de sedimento acima deste.

Uma primeira versão do sensor foi testada durante uma campanha de campo. Campanha esta em que também se recolheram dados experimentais acerca de processos ocorrentes na zona de rebentação e zona de swash. Posteriormente, estes dados foram analisados e processados visando uma melhor compreensão dos processos hidrodinâmicos aí decorrentes, culminando com o cálculo de valores de transporte sedimentares associados e variações topográficas/batimétricas, e subsequente comparação com medidas obtidas por outros métodos. Por fim, a caracterização das velocidades normais à linha de costa para um período referente a uma maré alta foi também efectuada.

Aos meus pais.

INDEX

Chapter 1: Introduction

1.1 Initial considerations, motivation and working objectives

The ocean floor is not visible to us, therefore it is difficult to map. For this reason, throughout the last centuries man has endeavoured the discovery of new techniques that would provide access to this terrain data that were previously inaccessible.

In the early 1800's, sailors took depth records in shallow waters with a weight on a line. Then, in 1854, a depth sounding device was attached to the line instead of the weight to improve the method; however, recording a small section of the ocean was time-consuming. During World War II, when submarine warfare was at its peak in the Atlantic and Pacific Oceans, sonar developed rapidly. After WW II, with the increased use of sonar, scientists were able to map ocean trenches, ridges, plains, and submerged islands. These maps were the critical first steps in the ocean discovery in the 1960's and 1970's. However, since the last decade of the twentieth century, there has been a major change in how the survey activities were made. Many of these changes came with the introduction of multi-beam echo sounder, an improvement to the existing single-beam echo sounder, and also the introduction of echo sounder with side scanning, the data storage in digital format, and the usage of GPS (Global Positioning System). These innovations have enabled a breakthrough technology, allowing the collection and data storage more efficient.

The coastal zone has an important influence on the well-being of communities, whose homes and industries lying along the coast are exposed to the existing wave action. For this reason, is well known the importance assumed by the characteristics of waves in studies related to coastline. The hydrodynamic processes involved play a major role in sediment transport across the coast and, consequently, in the changes of the nearshore bathymetric profile. However, this problem is far from being solved. Some of the reasons are pointed out: this region is highly dynamic, where complex processes like the modification of the wave profile and breaking occur simultaneously with bed changes; and there is a lack of field data (bathymetric changes included) due to its difficulty. Thence, the use of computers became crucial to analyse data, to model the coastal processes and the impact of engineering works, with a better understanding of, and concern for, the environment.

Alternatives have emerged to implement water depth and topographic measurements in the coastal areas. Among them are the innovative remote sensing systems such as airborne laser scanning (aerial – airborne or satellite - spaceborne), autonomous underwater vehicles - AUV's, video-monitoring systems or optical sensing systems based on fiber Bragg gratings optical fiber, such as that developed and described in this work.

In-fiber grating based sensors has many advantages over conventional electric and alternative fiber optic sensor configurations. They are simple to implement, low-cost to produce, immune to electromagnetic interference, lightweight, small in size, self-referencing with a linear response and, most notably, their wavelength multiplexing capability allows tens of gratings in a portion of fiber to form an optical databus network. These features and their inherent compatibility with fiber-reinforced composite materials allow in-fiber gratings to be embedded in a number of

important structural materials for structure applications. Undeniably, the development of structurally integrated fiber optic sensors, using fiber Bragg gratings (FBGs), represents a key contribution to the evolution of smart structures, leading to improvements in both safety and economics in many engineering fields, like major civil works, road and rail bridges, tunnels, dams, maritime structures, airframe sections, projectile delivery systems, and numerous medical appliances.

This thesis aims the development of an optical fiber sensor based in fiber Bragg gratings technology, capable of monitoring remotely and in real-time the bed level changes in nearshore regions, through the height measurement of the sediment column. It has also the objective of analysing and processing data from the swash zone (velocity flow and wave height), obtained in a field survey at Ancão beach, to better understand the hydrodynamics and sediment transport of that specific region, and consequently, to relate with nearshore bathymetric/topographic profile also measured with other techniques.

1.2 Thesis structure

This thesis is organized into seven chapters, being Chapter 1 the Introduction.

In Chapter 2 (State-of-the-art of technology capable to perform bathymetric and topographic measures) is made an overview of more common current technologies with the ability to perform depth and topographic measurements. For each of the technologies discussed is presented a brief description of itself, their operating principle, and main characteristics.

Within the confines of Chapter 3 (Waves and soil mechanics in the swash zone) it is possible to summarize some aspects of wave action and soil mechanics in the nearshore region, namely in swash zone. Thus, hydromorphodynamics phenomena are discussed and a description of the overall swash zone operation is given. It is also presented a configuration to simulate real conditions for a device buried in the sand on the same region.

Swash zone experimental data obtained during a campaign is presented in Chapter 4 (Processing and analysis of swash zone experimental data), which include all data processing and detailed results with posterior analysis and discussion.

In Chapter 5 (Technology Bragg gratings in optical fiber for use in sensors) are explained the fundamental concepts inherent to optical fiber and fiber Bragg gratings and, more specifically, all the main results to take into account during the document. Beyond this, it is summarized the recent state of optical fiber Bragg grating sensors implementation.

The sensor development process, as well as, the characterization of the final sensor version, is shown in Chapter 6 (Development of an optical pressure sensor using fiber Bragg gratings). Thermal, humidity and mechanical characterizations for simulated and real conditions were achieved too.

Finally, ultimate conclusions and future work is drawn in Chapter 7.

Chapter 2: State-of-the-art of technology capable to perform bathymetric and topographic measures

In recent years there has been a major change in the way that topographic and bathymetric survey activities have perform, due to the arising of new technologies or methods. Direct topographic surveys using levelling instruments such as theodolites, dumpy levels and clinometers, were surpassed by GIS technology that combine the usage of a GPS to georeference points in a certain area. On the other hand, the common employment of echo sounder for bathymetric measurements is becoming less used with the emergence of alternative remote technologies capable of becoming more effective, like airborne laser scanning - Lidars , which can also perform topographic surveys, Autonomous Underwater Vehicles - AUV's (for bathymetric surveys only), or optical systems based on, e.g., fiber Bragg gratings, as the one described in this thesis.

Regardless of all of these techniques, it must be taken into account that the technology used depends on the scale and size of the area under study, its accessibility, and the quality of existing surveys. The relation between the effectiveness/accuracy desired with the method used is something that must be kept in mind.

GIS-based topographic survey: The objective of topography is to determine the position of any point in terms of both a horizontal coordinate system such as latitude and longitude, and altitude. Despite the new remote sensing techniques that speeded up the process of gathering information and allowed greater accuracy control over long distances, the direct survey GIS-based (Geographic Information Systems) still provides the basic control points and framework for all topographic work [1]. Nowadays, direct surveys are performed with a GPS normally by feet, although, are being tested and developed independent systems to carry the GPS. Accuracies achieved with this kind of systems are of 10 cm (horizontal accuracy) [1] and 10 cm (vertical accuracy) [2].

Echo sounder: The employ of an echo sounder is currently the more conventional method to carry out bathymetric measurements, which can be single-beam or multi-beam. Being the last one is most effective to ensure full coverage of the desired area. GPS is practically the only technique used to position the probe during its journey, nowadays.

The operation principle of this equipment is based on the measurement of time, spent by an acoustic signal to pass through the distance between the transmitter and the sea bottom, and return to the receiver. It is essential to predetermine the speed of sound in water in order to calibrate the echo sounder. This can vary from about 1420 m/s to 1580 m/s, depending on temperature, salinity, and pressure [3, 4].

Airborne lidar bathymetry system: The term "lidar" is an acronym for LIght Detection And Ranging. It is an optical remote technology that measures properties of scattered light in order to determine the distance and/or other properties of certain distant target. It is similar to radar technology, standing the main difference in the use of laser pulses, instead of radio waves.

An Airborne Lidar Bathymetry (ALB) system uses lidar technology to measure water depths. A laser transceiver (transmitter/receiver) mounted on an airplane emits a laser pulse which travels to the air-water interface, where a portion of this reflects back to the receiver. The remaining

signal propagates through the water column and reflects off the sea bottom. The water depth measurement comes directly from the time lapse between the surface return and bottom return (Figure 2.1). In practical application of this technology, laser energy is lost due to refraction, scattering, and absorption at the water surface, sea bottom and as the pulse travels through the water column. The combination of these effects limits the strength of the bottom return and therefore limits the maximum detectable depth. The water clarity, for the signal, and the bottom types are the two most limiting factors for depth detection. Each measure of depth is related to a horizontal location at the instant of measurement obtained with a GPS [5, 6].

Table 2.1 An ALB system performance characteristics [7].

Maximum depth	to 40 m
Vertical accuracy	± 15 cm
Horizontal accuracy	± 3 m
Sounding density	4 to 8 m grid
Operating altitude	200 to 400 m
Scan Swath Width	110 to 220 m
Operating speed	115 to 230 m/s

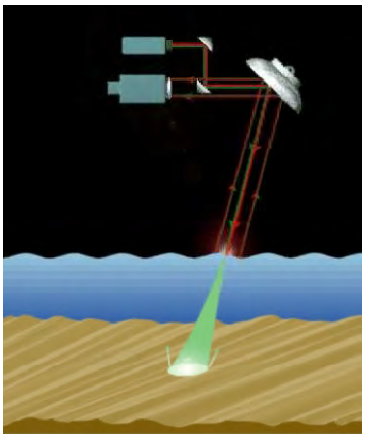

Figure 2.1 ALB operating principle [7].

Autonomous Underwater Vehicles (AUV's): An AUV is a robotic device that is driven along its path in the water by a propulsion system, controlled and piloted by an internal computer to any location in space. They were first developed with military applications in mind, namely for mine hunting missions. Later on, scientists realized their true potential and started to use them as mobile sensors, taking samples in difficult scenarios at a reasonable cost. For most of the environmental conditions, the level of control achieved allows the vehicle to follow pre-programmed trajectories (scripts) whenever and wherever needed [8].

Most of the AUV's do not process the information obtained through its sensors in real time, and therefore, do not use it for a continuous adjustment to the objectives, being only saved for future analysis. However, more recently, have been developed new vehicles with these capabilities, as well as the ability to cooperate with others on the ground, and so share a network in real time. Today, there are a wide variety of AUV's where can be emphasized the REMUS 100 (Remote Environmental Monitoring Units) shown in Figure 2.2.

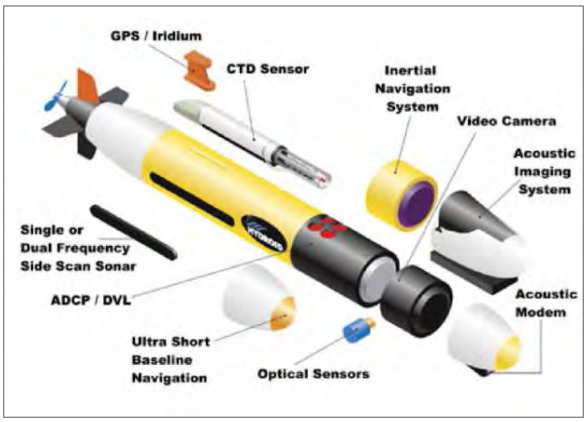

Figure 2.2 Schematic draw of an AUV REMUS 100 equipped with sensors [9].

The REMUS 100 is a lightweight, compact and low cost AUV specially designed to operate in coastal environments up to 100 m deep. Its small size and weight make this device easy to handle, don't requiring special equipment for its launch and subsequent recall. It can also be easily configured to include a wide variety of standard sensors and/or specific optional sensors in order to meet the pre-established objectives [8, 9].

Chapter 3: Waves and soil mechanics in the swash zone

3.1 Concepts of waves

Waves, generated primarily by the wind, propagate from the ocean to the shoreline across the continental shelves. These waves undergo many processes before they dissipate in the surf zone: refraction, diffraction, shoaling, and breaking. The energy and momentum associated with the waves arriving at the surf zone is used to create longshore and cross-shore currents that move the sand modifying beaches.

The basic parameters to describe a wave are its length, L, wave period, T, height, H, and the depth of which is propagating. All other parameters or quantities such as the orbital or wave-induced accelerations can be determined theoretically from these quantities. In Figure 3.1 is shown a schematic drawing of a wave propagating in the x direction [10].

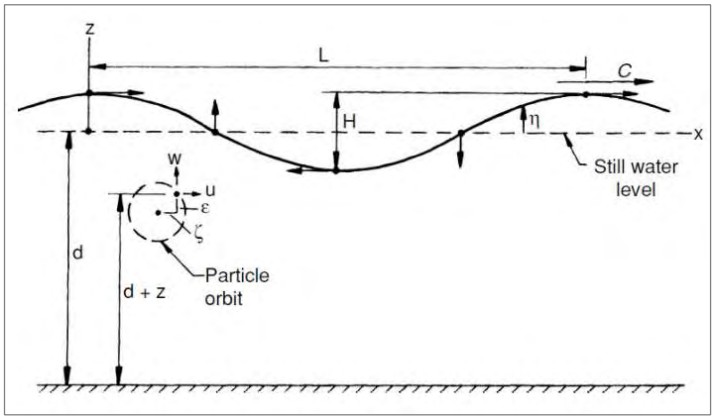

Figure 3.1 Wave schematic diagram and characteristic parameters [11].

As the incident waves approach more and more to the beach they become sharply peaked and with the troughs broad and flat. Moreover, just prior to and during wave breaking, waves become increasingly asymmetric, during wave transformation, with pitched forward, steep leading faces and more gently sloping rear faces. This results in strong fluid velocity accelerations under the steep leading face of the asymmetric wave [12]. This wave transformation is schematized in Figure 3.2.

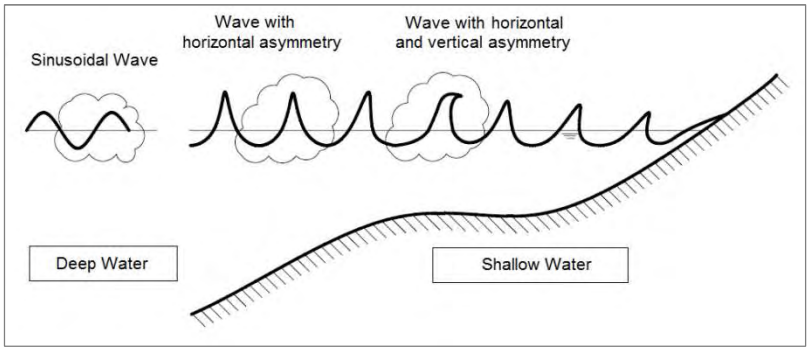

Figure 3.2 Schematic diagram of wave transformation when approaching the beach [13].

3.2 The swash zone

It is widely acknowledged that the majority of coastal sediment transport occurs in the nearshore zone, including the wave-breaking zone, the surf zone with predominantly broken waves and the swash zone characterised by wave uprush and backwash. Although only occupying the innermost part of the nearshore zone, the swash zone is a region of high flow velocities and disproportionately high sediment transport. Considerable efforts have been made to improve the state of knowledge of swash zone hydrodynamics in recent years, though it remains poorly understood.

The oscillatory flows of the swash zone are characterized by two main properties: i) intermittency, i.e., the moving shoreline leads to alternate wet and dry regions across the beach face where the flow depth and velocity are only defined for short intervals of time; ii) shallow depths, i.e., the collapse of the flow moving to shoreline leads to shallow depths throughout the swash zone, shallower in comparison to the horizontal length scale of the flow. In these shallow intermittent flows, descriptions of the bed boundary layer and friction remain a challenge despite recent progress. In oscillatory wave boundary layers, the effects of friction in terms of energy dissipation and net sediment transport are usually described in terms of a constant friction factor over the wave period. However, this is not appropriate for swash zone flows, where the initial conditions and flow depths for the uprush and backwash flows are very different [14].

A brief description of the swash zone dynamics induced by breaking waves is qualitatively illustrated through Figure 3.3 and 3.4. Here, x_l and x_h are the lowest rundown and the highest run-up, respectively, during a cycle. On the other hand, the arrows at mid water depth indicate the intensity of the depth-averaged velocity, and the arrows at the bed indicate the direction of the water flow in the bed (downward indicates infiltration; upward indicates exfiltration).

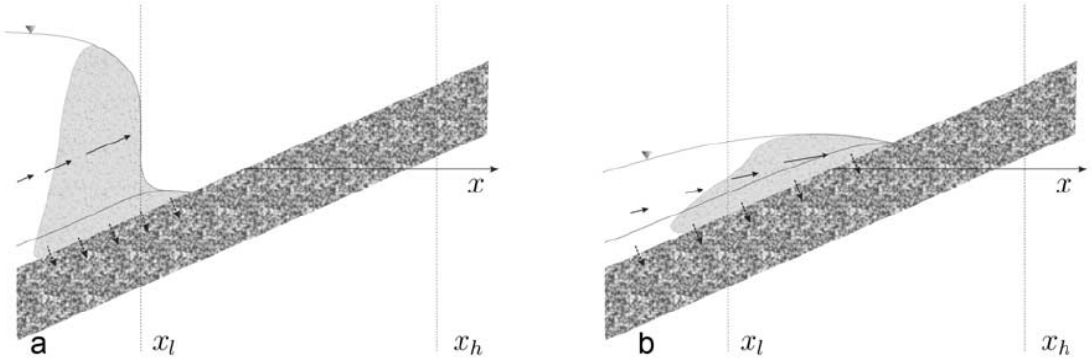

Figure 3.3 Run-up phase of a swash event. (a) Bore collapse at $t = 0$. (b) Run-up at $t \approx 2\,T_s/10$, where T_s is the natural period of the individual swash events [14].

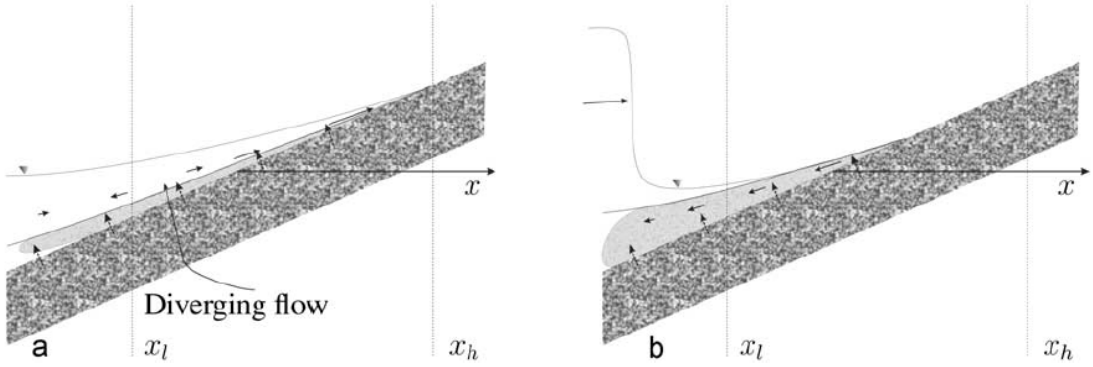

Figure 3.4 Run-down phase of a swash event. (a) End of the run-up and beginning of rundown at $t \approx 4\,T_s/10$. (b) Rundown and following incoming wave at $t \approx 8\,T_s/10$ [14].

Example of the typical temporal variation of swash flow depth, h, and bed-parallel velocity, U_x, are presented in Figures 3.5, during one wave period, and also in Figure 3.6 during a larger period of time and covering a few number of waves.

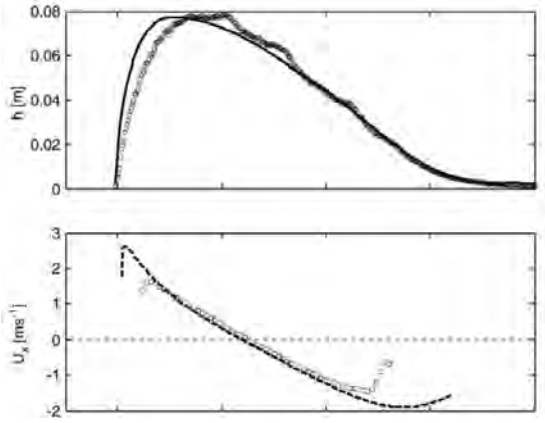

Figure 3.5 Measured swash flow depth, h, and horizontal velocity component U_x by Barnes et al. [15]. The solid (h) and dash (U_x) lines represent modeled parameters.

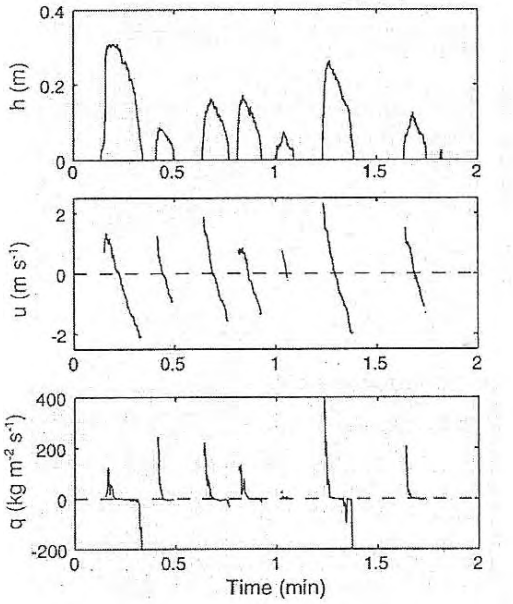

Figure 3.6 Example time series of water depth, h, flow velocity, u, and sediment transport rate, q,in the mid-swash zone on Sennen beach [16].

3.3 Concepts of soil mechanics

Much of the Earth's surface, either in submerged vast areas, or in areas emerged, is covered by soil. These masses are formed by mineral particles that resulted from the physical disintegration and the chemical decomposition of rocks, containing also organic matter. Soil particles pack loosely, forming a soil structure filled with empty spaces or pore spaces. These pores may contain water (liquid) and air (gas), alone or in mixture. Whenever the pores are completely filled with water is said that the soil is saturated.

The most basic characteristic of a soil is its soil texture, defined as the distribution in percentage weight of the soil grains according with their sizes. For larger particles the conventional method to determine soil texture is using sieves, whereas for smaller particles, the commonly method used is sedimentation. In soils, the grain size of sediment can vary by several orders of magnitude, ranging from gravel and sand to very small particles classified as clay and silt. A table, with the classification of sediment in what its size (diameter) concerns, is shown below [17].

Table 3.1 Sediment classification as function of grain size (mm or ϕ), with $\phi = -\log_2(D/1\text{ mm})$.

Type	Range of values	
	(mm)	(ϕ)
Gravel	> 2 mm	< -1 ϕ
Sand	0,063 – 2 mm	4 – -1 ϕ
Silt	0,004 – 0,063 mm	8 – 4 ϕ
Clay	< 0,004 mm	> 8 ϕ

Granular soils, or simply sand, is the name of soils where there is a predominance of coarser particles namely gravel and sand. These are, precisely, the type of soil that can be encountered in beaches, which are the regions of particular importance for this work. Therefore, it is of full

interest to present some important properties that the grains of these types of soils have, like: they are constituted mainly by quartz, which is chemically very stable; they are approximately equidimensional, i.e., taking three mutually orthogonal directions, they are generally of the same order of magnitude; and, as good approximation, all the sediments are considered as non-cohesive. These properties imply that: the interaction force between each particle with the external environment is, almost exclusively, of the gravitational type; the spherical shape of the grains can be taken as the simplified model of each particle; and, the sediment density can be approximated to the density of quartz, i.e., $\rho_s = 2650\ \mathrm{Kg/m^3}$ [18].

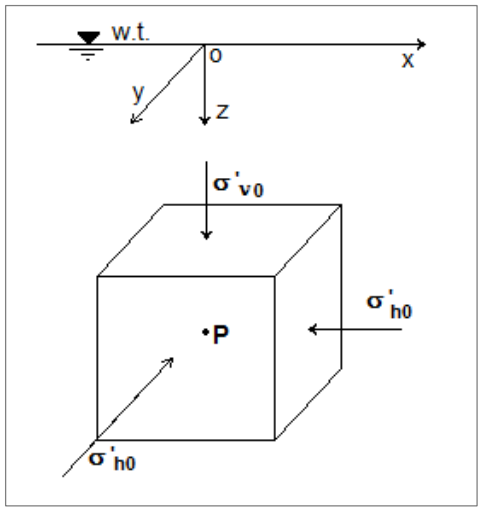

Figure 3.7 Effective static stresses in an infinitesimal point into the soil with horizontal surface [18].

Therefore, the static stress state of a soil with horizontal surface is just evaluated by the tensions arising from its own weight. Consider then a homogeneous sandy soil with horizontal surface represented in Figure 3.7 with density, ρ_s, constant in depth. Consider also, for simplicity, that the ground water encounters in equilibrium and in steady conditions (distribution of hydrostatic pressure), with its water table coincident with the soil surface. Consider an infinitesimal point, P, with its three pairs of facets normal to the coordinate axes. In these facets the stresses are solely normal to them, and so these directions are named the main stresses directions.

The total vertical stress at P acts on the horizontal facets and is given by,

$$\sigma_{v0} = \rho_s g z \tag{3.1}$$

with the index "zero" meaning that the stress is exclusively due its own weight. Moreover, being the water in hydrostatic conditions and the water table at soil surface, the pore pressure at P is

$$p_p = \rho_w g z \tag{3.2}$$

where p_p is the pore water pressure which refers to the pressure of groundwater held in gaps between particles (pores), within the soil. The assumption that this pressure would be close to hydrostatic in no flow conditions, is valid for a high permeability soil like a sandy soil of a beach. From equations 3.1 and 3.2 arises then that the effective stress at the point P is given by

$$\sigma'_{v0} = (\rho_s - \rho_w) g z \tag{3.3}$$

where this equation represents the nominated effective stress principle [18]. This concept is one of Karl Terzaghi's most important contributions to soil mechanics, since it is a measure of the stress on the soil skeleton (the collection of particles in contact with each other), that determines the ability of soil to resist shear stress. Notice that it cannot be measured in itself, but must be calculated from the difference between two parameters that can be measured or estimated with reasonable accuracy, like the total stress, σ_{v0}, and the pore pressure, p_p. The pore pressure can be measured with the help of a piezometer, when deployed at the point in study. Finally, at the vertical facets in the Figure 3.7 the acting stresses (horizontal stresses) will be naturally all equal between them. Unlike vertical stresses, its calculation doesn't result from only gravitational

considerations, and it is necessary to define the coefficient of lateral stress, Λ, based on effective stress as, $\Lambda = \sigma'_{h0}/\sigma'_{v0}$ [18].

Another topic of interest related with soil mechanics in the swash zone is the wave-induced pore pressures in the seabed. This has been an item for extensive research since it has an influence on the geotechnical stability of structures and may also have an effect on the transport of sand. Thus, considering that above of the point P there is a certain wave regime, the pore pressure at that point should be given by equation 3.2 plus a contribution originated from the waves above it. Although detailed field observations of pore pressure in the surf zone are scarce, as a result of the difficulties of taking measurements in the breaking zone, in recent years, several studies attempted to take accurate pore pressure measurements in this zone, like the one described in Michallet *et al.* [19].

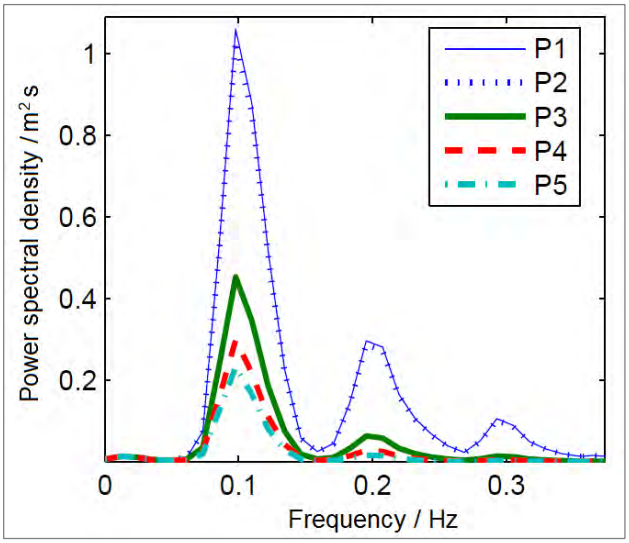

Figure 3.8 Power spectral densities of water pressure variations measured simultaneously by five pressure sensors [19].

In this specific study five pressure sensors were deployed with a spacing of 30 cm from each other in a vertical bar embedded in the sandy bottom. The properties of waves were determined using the pressure sensors in the water layer, and the transmission of pressure variations inside the soil was analysed, in terms of both amplitude decay and phase shifts, by comparing the pressure variations measured at different levels inside the soil, P_3 to P_5, to those measured in the water layer, P_1 and P_2 (see Figure 3.8). It is first shown that the damping increases with increasing depth, and also the similar trends are observed for the phase shift. It was concluded that the greater the damping between two pressure sensors, the greater the phase shift between the pressure signals, the transmission of wave induced pore pressure inside the soil is a linear process.

Beyond this, the results also confirmed that the gas content is a parameter affecting the transmission of pressure inside the soil. This gas is introduced in the soil at low tide and remains partly trapped inside the soil unless particle movements let the gas escape during the tide. Site air content measurement and its time variation during a tide period may provide information and help to determine a better understanding of this phenomenon.

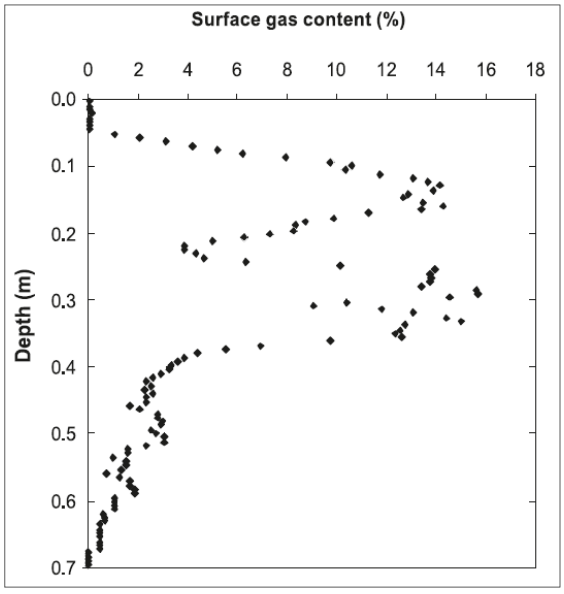

Figure 3.9 Surface air content ratios versus depth [20].

As described by Breul *et al.* [20], techniques based on a geoendoscopy and automatic image analysis makes possible to characterize coastal

soils and to estimate their air content. The results presented in Figure 3.9 were obtained as a result of the geoendoscope being in a fixed position during one tide. From regularly acquired images, could be accessed after image processing the evolution of the quantity of air trapped in the ground during the tide. The major result is the proven existence of a significant presence of air deep inside the soil, and it is not constant according to the depth as can be seen. A thin layer of satured soil is observed in the upper part of the sea bed.

3.4 Simulating a beach soil

To simulate in the laboratory the soil mechanics of a sandy dry soil, as can be found on a beach, it was thought of using a vertical cylinder filled with sand like the one schematized in Figure 3.10. According with Janssen's theory [21], proposed by him in 1895, the pressure measured at the bottom does not depend upon the height of the filling, i.e., it does not follow the law

$$p(z) = \rho g z \tag{3.4}$$

that would follow a fluid filling the cylinder, or as equation 3.1 says. The pressure in the granular material follows instead a different law, which accounts for saturation, given by

$$p(z) = \frac{\rho g L}{\mu}\{1 - e^{(\mu z/L)}\} \tag{3.5}$$

where the saturation pressure is $p_{sat} = \rho g L/\mu$, and μ is a parameter dependent on the grain characteristics.

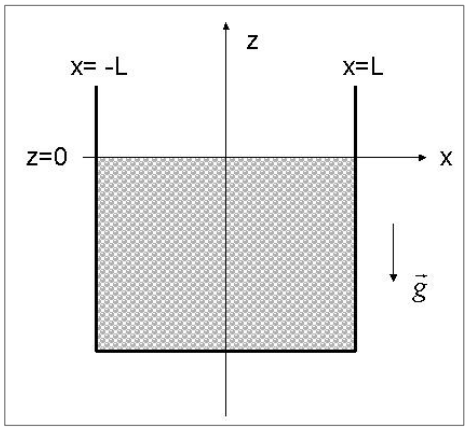

Figure 3.10 Schematic diagram of a vertical cylinder filled with sand, to simulate beach soil [22].

So, comparing qualitatively the real pressure response under a granular soil with the response obtained with the described configuration, can be concluded that the use of a vertical cylinder is a good simulation of reality for relatively low pressures. This can be seen in Figure 3.11, where the plot region inside the red circle shows that the pressure response is approximately the same. This result will be used further, in Chapter 6.

This law is very important in the framework of silos building, as the difference between ordinary hydrostatic and granular hydrostatic is mainly due to the presence of anomalous side pressure, i.e. force exerted against the walls of the cylinder. It happens that the use of a fluid-like estimate of the horizontal and vertical pressure leads to an underestimating of the side pressure and, consequently, to unexpected explosions of silos.

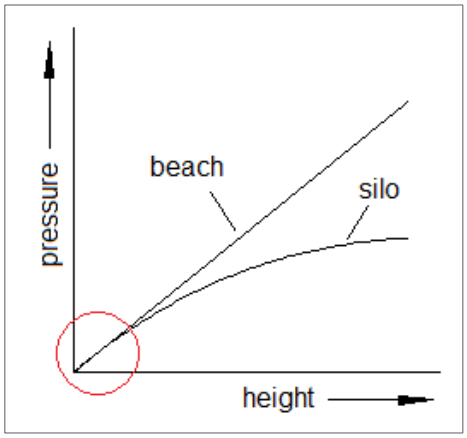

Figure 3.11 Comparison between vertical pressure responses at the beach and inside a silo.

Chapter 4: Processing and analysis of swash zone experimental data

This chapter is intended to present some of the results obtained during the first campaign of the Project BRISA: BReaking waves and Induced Sand transport. The campaign occurred between the 25th and the 28th of March 2009 at Ancão Beach in Algarve (south Portuguese coast). Velocity and sea surface water level data were collected in the breaking and swash zone through ADV's (Acoustic Doppler Velocimetry) and PT's (Pressure Transducer). Also topographic field measurements were made during along the entire campaign with a RTK GPS (Real Time Kinematic GPS).

4.1 Experimental setup

For the purpose of this thesis, only the data collected by one ADV in the swash zone and a pressure transducer nearby, as shown in Figure 4.1, will be considered and analysed. In the end, topographic surveys results obtained with the RTK GPS will be compared with post-processed data from ADV. The location of these devices in the field campaign can be seen in Figure 4.2 (blue arrow).

Figure 4.1 Photo of the used ADV and PT transducer.

Figure 4.2 Schematic localization of the instruments and correspondent beach profiles

An ADV is designed to record instantaneous velocity components at a single-point with a relatively high frequency. The principle of operation is the measure of the velocity of particles in a remote sampling volume based upon the Doppler shift effect. The ADV used during the campaign operates at 10 MHz, the maximum speed was set to 2,5 ms^{-1}, the sampling rate was 20 Hz, and the distance from the transmitter to the remote sampling volume is about 11 cm.

4.2 Data analysis during one tidal cycle

During the campaign were collected four ADV data files associated with different high tides that are exhibited in the Table 4.1. For the objectives of this thesis, from all the data files only one was chosen to be analyzed, the ADVA270102 correspondent to the second high tide. An example time series of 100 seconds of cross-shore, U_x, and along shore, U_y, velocities are presented in Figure 4.3: the black colour line represents the raw data, and the red the withdrawn wave data

after applying a filter that enable to identify each wave. The XOY coordinate system is represented in Figure 4.2. On the other hand, Figure 4.4 presents both the cross-shore velocity, U_x, and the height of water obtained with the PT for other different illustrative time series.

Table 4.1 Data collected with the ADV.

Day	File	Tide	Beginning	End	Total data collected	Transmitter-bed distance	
						initial	final
26	ADVA261320	1	13:20	15:42	169903	17,0	17,5
27	ADVA270102	2	01:04	05:12	207968	19,5	18,5
	ADVA271311	3	13:12	16:13	205166	19,5	17,5
28	ADVA281340	5	13:44	15:59	161488	18,5	-----

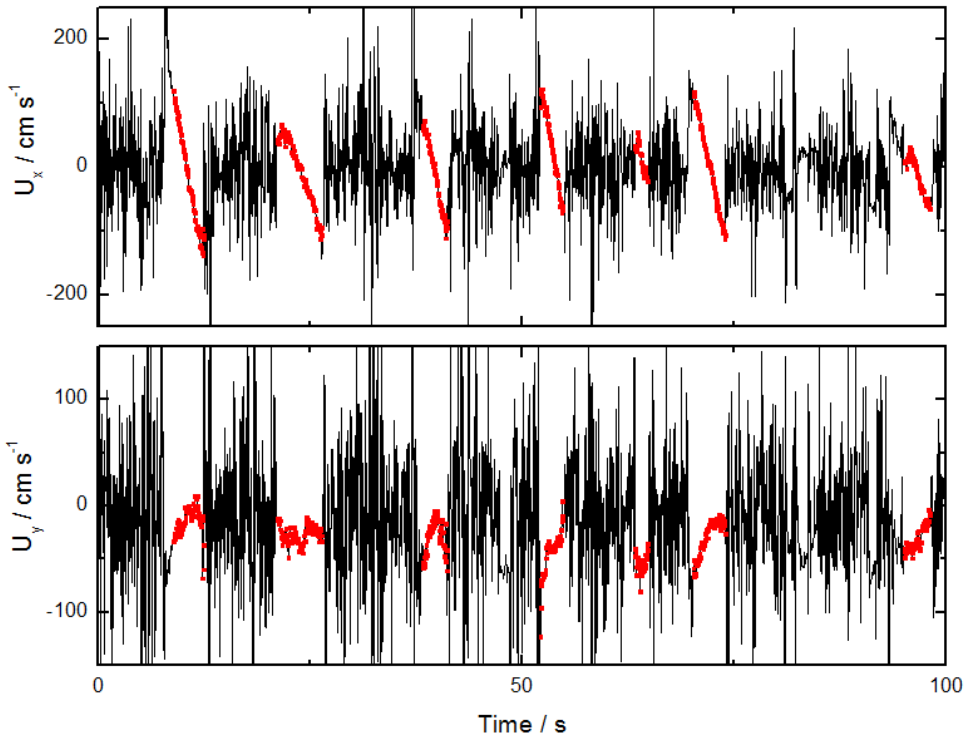

Figure 4.3 Example time series of cross-shore velocity, U_x, (up), and long-shore velocity, U_y, (down) during the campaign (ADV270102). The red points are the wave data after a filtering process, and in black raw data.

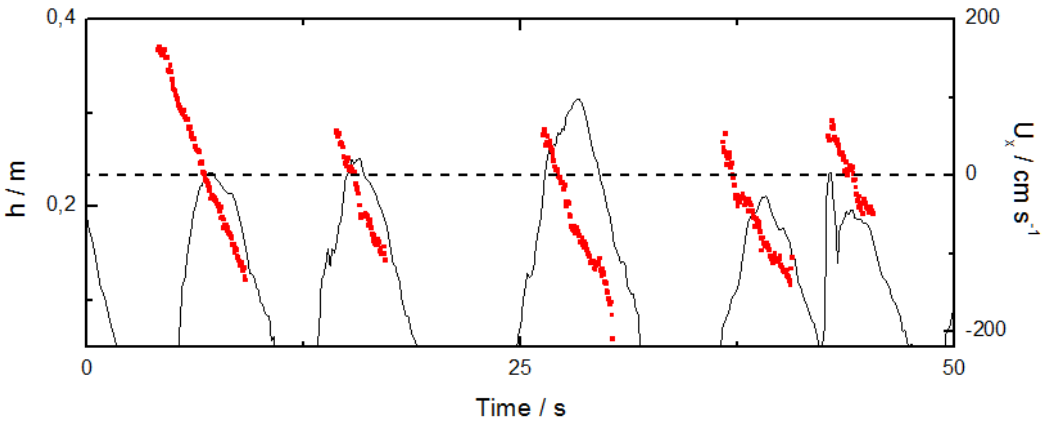

Figure 4.4 Example time series of water depth, h, (black line - obtained with the PT) and flow cross-shore velocity, U_x, (red points - obtained with the ADV) during the campaign.

Comparing these graphs with the represented in Figure 3.5 and 3.6, is possible to see that the experimental data is totally in agreement with the expected, in what cross-shore velocity concerns. It is also possible to infer that the data acquired through the pressure transducer is completely in conformity with the ADV data. The recorded swashes are characterized by maximum flow velocities range between 0,5 and 1,5 m s^{-1}, with maximum onshore and offshore velocities occurring, approximately and respectively, at the start of the uprush and the end of the backwash. Flow reversal coincides approximately with the time of maximum swash depth, which is around 20 cm reaching maximum values of about 30 cm. On the other hand, the along-shore velocity is practically always negative, which means the waves weren't breaking at right angle with the beach inducing a mean. Flow was from northwest to southeast.

However, it should be borne in mind that the water depth and flow velocity were recorded at different points in the water column (see Figure 4.1). The pressure transducer acquired data at 3 cm from the bed, and in other hand, the ADV collected data at, approximately, 8 cm from the bed (see Table 4.1). In addition, the transmitters of the ADV, which are at ~19 cm from the bed, must be totally immersed to be possible to the ADV gather data from flow velocity. This justifies why not all of the wave-flow velocities were recorded.

4.3 Waves characterization

To characterize the wave pulses, the corresponding cross-shore velocity measured by the ADV were analysed. For that purpose, some parameters were computed, such as: the maximum and minimum cross-shore velocity with respective occurrence time; the mean long-shore velocity; the wave period; the time during positive half-cycle of the wave, t_1, corresponding to the uprush; the time during negative half-cycle of the wave, t_2, corresponding to the backwash; the cross-shore velocity skewness, u^3, and kurtosis, u^4; and, at finally, the parameter R related with cross-shore velocity skewness and defined as

$$R = \frac{U_{x,max}}{U_{x,max}+|U_{x,min}|}. \tag{4.1}$$

Some of these quantities are shown in Figure 4.5. Note that skewness and kurtosis are defined as the third and fourth moment, respectively, of a quantifiable parameter such as fluid velocity, and they are used to describe the evolution of a shoaling surface gravity wave as the wave crests become sharply peaked and the troughs broad and flat. Thus, these parameters are commonly used to parameterise the wave-shape evolution [12].

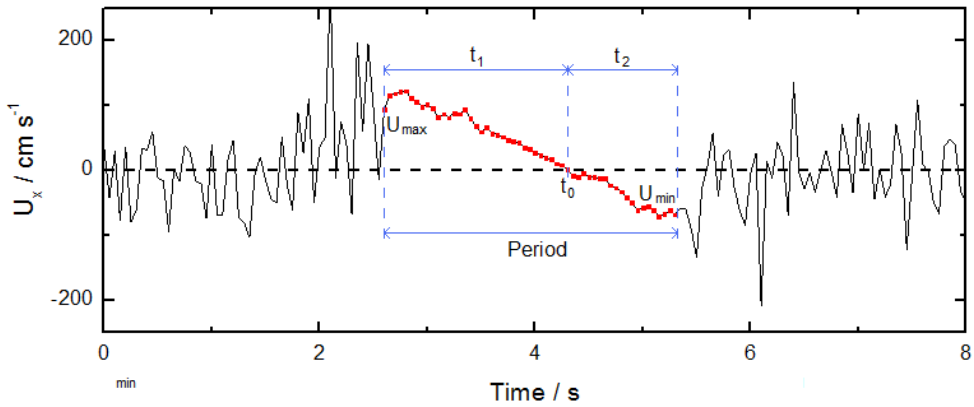

Figure 4.5 Definition of parameters for the cross-shore velocity wave pulses in the swash zone.

Not all of the identified waves have a typical or regular behaviour. Subsequently, it was required to choose among them (by applying created logic conditions) those waves for which the parameters described above were undoubted determined. This resulted in a set of waves to be taken into account for further calculations. Example of waves that weren't considered were waves with two different zeros, or waves with relative maximums or minimums in flow-velocity. Hence, the percentage of waves not considered was around 10 %.

Now, the parameter analysis for the chosen high tide can be performed. For that purpose, the means values of the parameters in sequential groups of 10 minutes each were calculated. For each group a different number of waves were identified. This information is provided in Figure 4.6. Note that although in Table 4.1 the time duration of whole ADV record is around 4hours, only during 160 minutes (2 hours and 40 minutes) the water level at the ADV enabled velocity measurements. The water depth measured in the surf zone is presented in Figure 4.7 showing the evolution of the tide, and when it reached its maximum level.

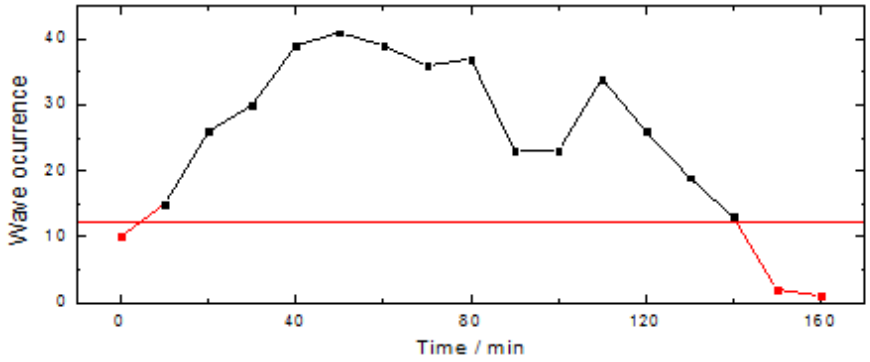

Figure 4.6 Waves occurrence (frequency) in data groups of 10 minutes. Below the red line (which represents 30% of the maximum value of the graph) the wave frequency is not significant. Thus, data related with this 10 minute-group are also non-significant and will always appear in red colour in the following graphs.

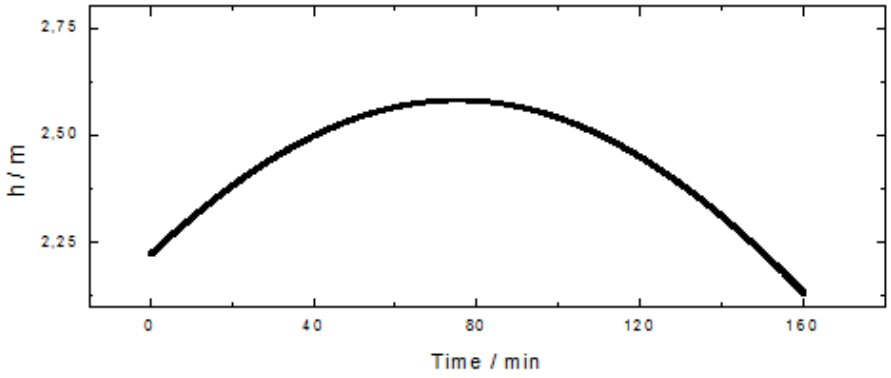

Figure 4.7 Water depths in surf zone during the tide which data relates (ADV270102).

Observing the last two figures, it is evident that wave occurrence is higher when the tide is close to its maximum. Between 10 and 40 waves were found, in general, for each data group of 10 minutes. This graph is important to evaluate the parameters calculations shown in the next figures. The points marked in red colour shown in the following graphs are not significant due to lack of ADV data, in accordance with Figure 4.6.

Figures 4.8 and 4.9 present the maximum and minimum values of the cross-shore flow velocities: the maximum cross-shore velocity, $U_{x,max}$, (uprush) don't suffer big modifications and it is, in general, between 75 and 100 cm s^{-1};on the other hand, the minimum cross-shore velocity,

$U_{x,min}$, (backwash) suffer more significant changes, as it has values ranging from -50 to -110 cm s^{-1}. This information is implied in the parameter R, shown in Figure 4.10, since it is defined as a relation between maximum and minimum cross-shore velocity (see equation 4.1). So, in general, the parameter R is close to 0,5 when the tide is near its maximum value (from minute 40 to minute 130), meaning that the flow velocity is quite symmetric during these periods. However, it is higher than 0,5 for lower tidal level. Thus, it can be concluded that R changes are mainly related with minimum cross-shore velocity.

Regarding the along-shore velocity, U_y, it is almost constant during the time of acquisition meaning that the direction of the flow didn't change significantly during the all tidal cycle. This is illustrated in Figure 4.11. At last, notice that the standard deviation points (green points in the figures) are roughly regular for all the graphs.

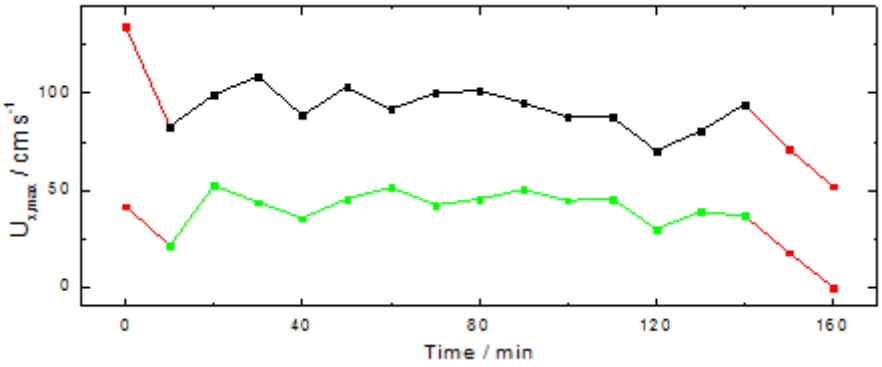

Figure 4.8 Evolution of maximum cross-shore velocity, $U_{x,max}$, during tide (black), and respective standard deviation (green).

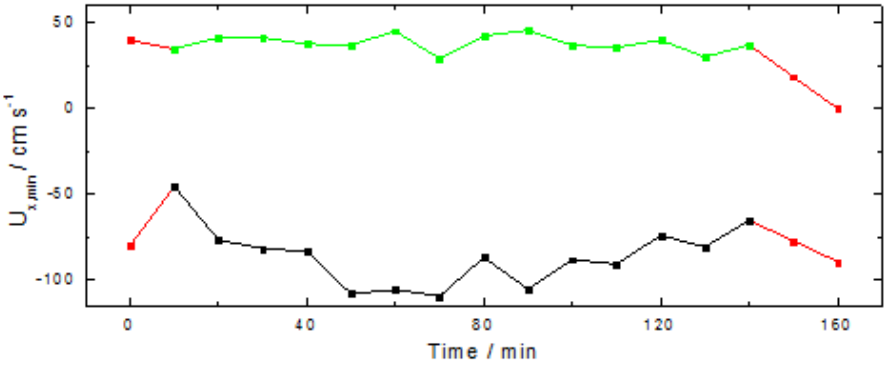

Figure 4.9 Evolution of minimum cross-shore velocity, $U_{x,min}$, during tide (black), and respective standard deviation (green).

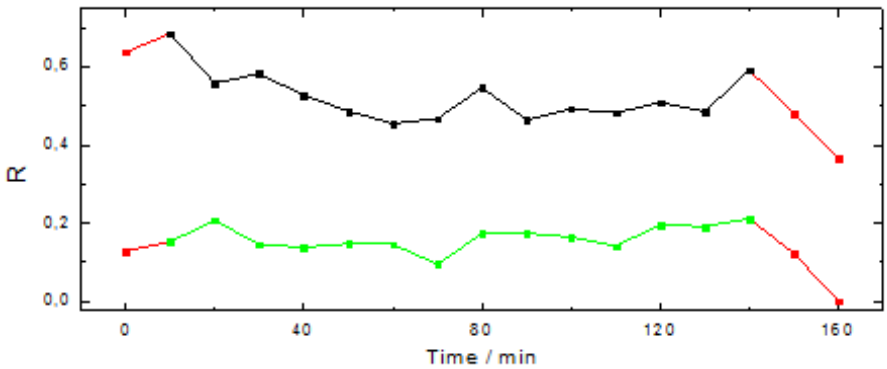

Figure 4.10 Evolution of parameter R during tide (black), and respective standard deviation (green).

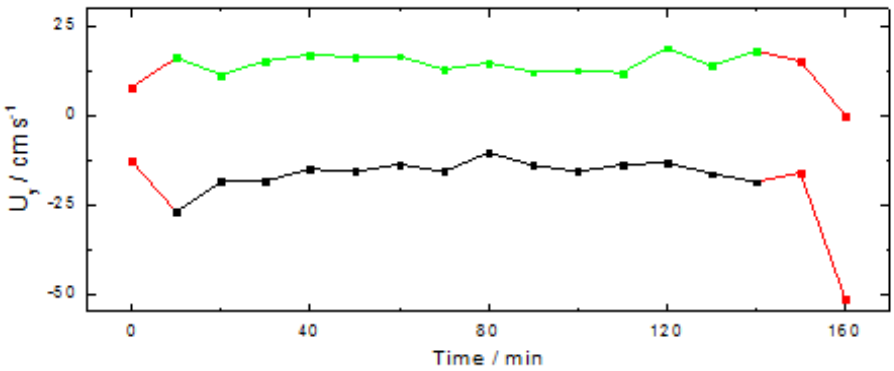

Figure 4.11 Evolution of along-shore velocity, U_y, during tide (black), and respective standard deviation (green).

Figure 4.12 shows the evolution of the period, T, as well as the evolution of positive and negative half-cycle periods, t_1 and t_2, respectively (see Figure 4.5 for definitions). Analysing the graphs it is evident that the period of wave is higher for higher tide levels. The positive half-cycle period doesn't diverge very much along the tide (violet colour), but, on the other side, the negative half-cycle period varies significantly during the same tide (blue colour). This implies that the perceptible changes in the wave period time are due, to a large extent, to changes in the semi-period t_2.

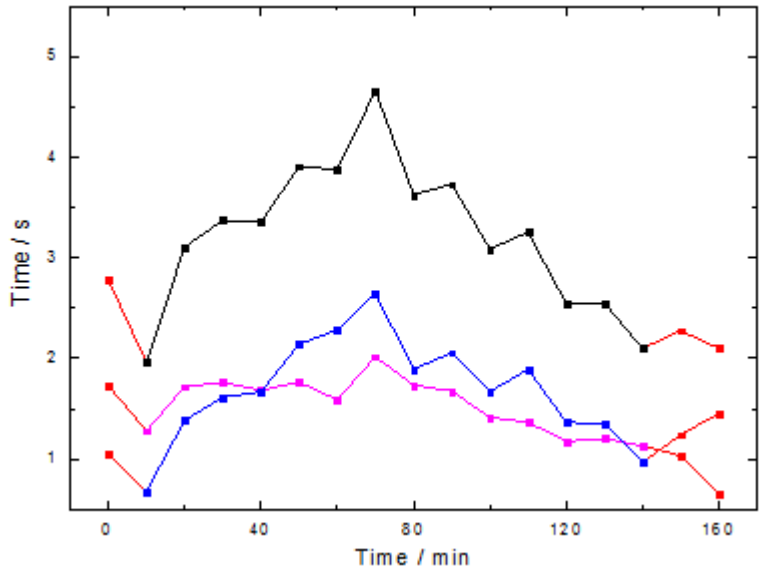

Figure 4.12 Evolution of wave period during tide, T, (black), wave positive half-cycle period, t_1, (violet) and wave negative half-cycle period, t_2 (blue).

Finally, and observing the respective figures of the velocity skewness and kurtosis, Figures 4.13 and 4.14, respectively, arises that both curves have similar trends. The values are predominantly slightly positive during lower water levels and tend to become around zero, or slightly negative, at high water levels. Since these parameters are a way of measure the asymmetry of the waves, they are also related with the parameter R graph and the same conclusions can be taken.

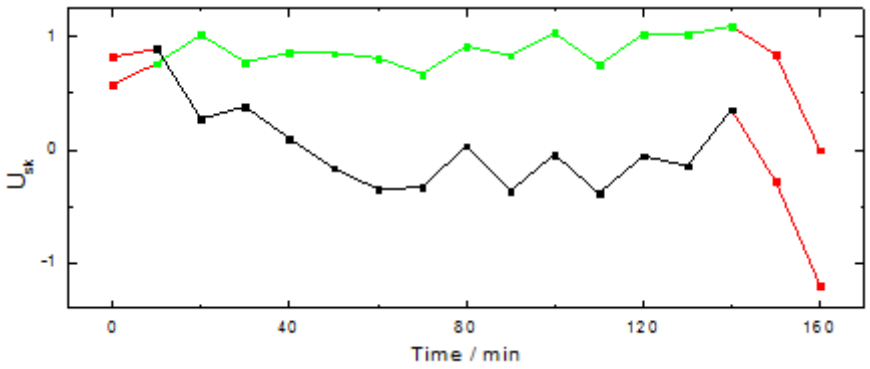

Figure 4.14 Evolution of skewness during tide (black), and respective standard deviation (green).

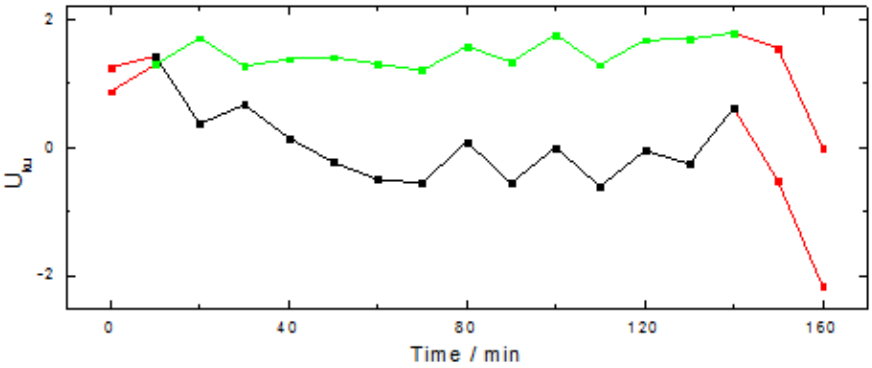

Figure 4.15 Evolution of kurtosis during tide (black), and respective standard deviation (green).

Although the variability of the wave parameters is noticeable as shown in the figures above, it would be interesting to evaluate an equivalent wave for the complete tidal cycle. As a result, it can be discussed if the approximation of considering a characteristic/equivalent wave for the all tide is a good approximation or not in what sediment transport concerns (see section 4.5). For that, the mean (weigh) values and respective standard deviations of all parameters were calculated for the set of chosen waves, and the results are shown in Table 4.2.

Table 4.2 Parameters values for ADV270102, with respective mean and standard deviation.

Parameter	Mean	Std. deviation
$U_{x,max}$ / ms^{-1}	94,3	44,2
$U_{x,min}$/ ms^{-1}	-89,4	40,9
$\overline{U}_y$/ ms^{-1}	-15,5	15,0
T / s	3,38	1,50
t_1 / s	1,59	0,78
t_2 / s	1,79	1,03
u_{sk}	-0,02	0,91
u_{ku}	-0,02	1,52
R	0,52	0,17

The characteristic wave found obtained is presented in Figure 4.16. It was computed through a quadratic fit to the three points represented in black. In section 4.5, this equivalent wave will be used to estimate the sediment transport during the complete tide to which data relates.

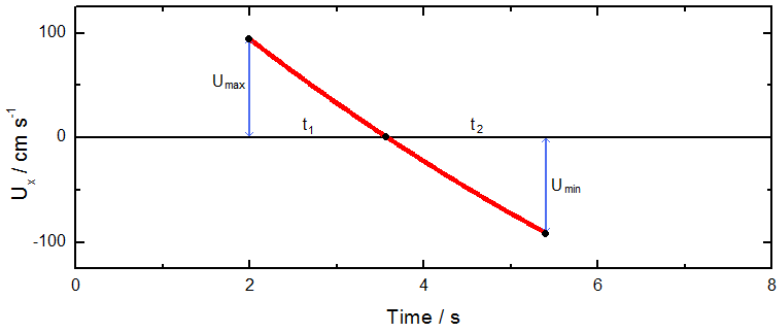

Figure 4.16 Equivalent swash zone wave for the second tide of the campaign (ADV270102).

4.4 Topographic data

Beyond the acquisition of ADV and PT data, topographic surveys were also done during the entire campaign (from 26 to 28 of March) at every low tide (see Table 4.3). The field area was surveyed with RTK GPS along 11 cross-shore profiles and 8 long-shore lines; however, only one profile, P4, (see Figure 4.2) is important for the purpose of this work. The evolution of this profile is shown in Figure 4.17.

Table 4.3 Topographic data acquired.

Survey number	Between tides	Day	Time
1	0-1	26	08:11
2	1-2	26	20:23
3	2-3	27	08:43
4	3-4	27	20:57
5	4-5	28	09:16
6	5-6	28	20:39

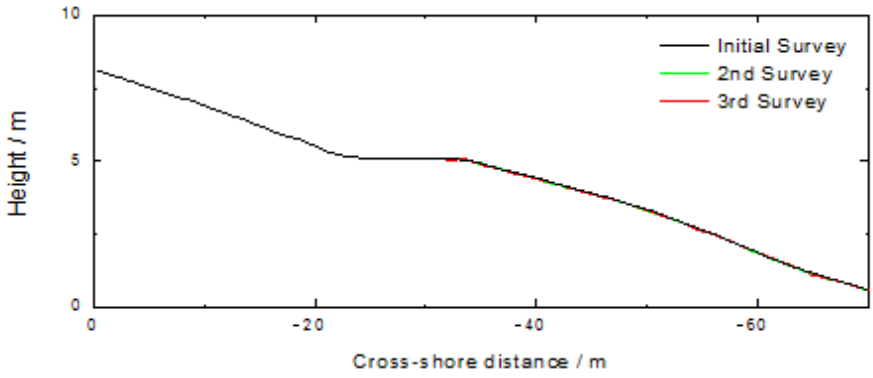

Figure 4.17 Cross-shore profile P4 changes along the campaign (distances are measured to a reference point in land).

Notice that the reference survey plotted in black in the figure above (March 26 at 8:11) was made along the entire grid. The undetectable variation of the cross-shore profiles in the upper part of the beach was the reason for the rest of the surveys (green and red lines) just covered the lower part of it. Figure 4.17 shows that the beach morphology didn't change significantly for the period in analysis (2nd and 3rd surveys). A detailed graph of the profile is presented in Figure 4.18. With this data it is possible to estimate the volumetric sand changes that took place in the near region where the ADV was placed ($x \approx -42$ m) during the 2nd tide. Posterior comparison with the

same quantity calculated through the data obtained with the ADV is presented in the next section.

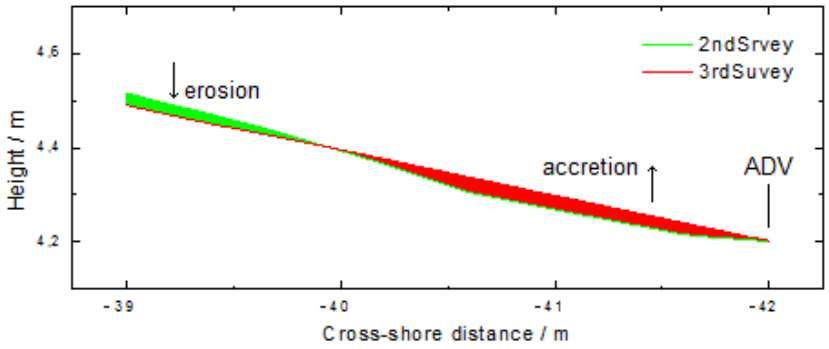

Figure 4.18 Detail of topographic data in the region near the ADV.

Figure 4.18 shows that inland to the site where the ADV was placed it was observed a few centimetres (between 1 and 5 cm) of accretion (red area), and for $x < -40$ m it was observed a small amount of erosion with changes of around 2 cm (green area). This is the region of major importance of the graph presented in Figure 4.17, since with the ADV/PT data it is only possible to estimate the volumetric sand changes inland to this particular point. For that purpose, it was assumed that the range of bed level changes related with measures taken with the ADV is 3 meters, between -39 and -42 m. Determining the area difference between the two surveys, a total accretion of ~0,03 m² per meter of beach width was achieved. This corresponds to about 80 Kg per meter of beach width of sand transported during the tide analysed, i.e., a small positive sand transport was noticed. Although the numerical value achieved, it can be concluded that practically there were no changes in the topographic level.

4.5 Sediment transport

Over the past few decades, important advances have been made in sediment transport modelling on-offshore (cross-shore) in the surf zone. Energetics-based models like the formulation of Bailard [23], in particular, which consider sediment transport as a function of higher-order velocity moments (velocity skewness, $u^3 \equiv u_{\mathrm{sk}}$, and velocity kurtosis, $u^4 \equiv u_{\mathrm{ku}}$), are able to predict nearshore bar formation and offshore bar migration under energetic wave conditions quite well. Given its relative success in the nearshore, it seems opportune to apply energetic models to the swash zone in an attempt to predict shoreline erosion and/or accretion, like Masselink *et al.* [16,24] or Emmanuel *et al.* [25] have done.

According to Bailard, the cross-shore sediment transport rate is given by:

$$q = q_b + q_s = \rho C_f \frac{\varepsilon_b}{\tan\phi}\left[|u|^2 u - \frac{\tan\beta}{\tan\phi}|u|^3\right] + \rho C_f \frac{\varepsilon_s}{w_s}\left[|u|^3 u - \frac{\varepsilon_s \tan\beta}{w_s}|u|^5\right] \tag{4.2}$$

where q is the immersed weight sediment transport rate, the subscripts 'b' and 's' indicate, respectively, bedload and suspended load, ρ is the density of seawater ($\rho_s = 1000$ Kg m^{-3}), C_f, is a friction coefficient which will be discussed further, u is he cross-shore current velocity, w_s is the sediment fall velocity ($w_s = 0{,}05$ m s^{-1}), ε is an efficiency factor ($\varepsilon_b = 0{,}135$; $\varepsilon_s = 0{,}015$), $\tan\phi$ is the tangent of the internal angle of friction ($\tan\phi = 0{,}63$), and $\tan\beta$ is the bed slope. The values for

the constants w_s, ε_b, ε_s and $\tan\phi$ were taken from Masselink *et al.* [16], and are also used by Emmanuel *et al.* [25]. Cross-shore bed gradient, $\tan\beta$, was determined thanks to the topographic data obtained between tides shown in the last section. The value assumed for the bed gradient in the ADV position is $\tan\beta = 0{,}10$. It should be noticed that the bed slope terms in equation 4.2 (with $\tan\beta$) have a relative weight much lesser than the other terms.

Hence, the transport rate, Q, is derived from the immersed weight transport rate using,

$$Q = \frac{q}{g(1-n)} \tag{4.3}$$

where Q has units of Kg s^{-1} per unit meter beach width (or Kg m^{-1} s^{-1}), g is the gravity constant ($g = 9{,}8$ m s^{-2}), and n the pore space assumed equal to 0,4.

Energetics-based models, like the Bailard model previously presented, rely on the assumption that q is related to the instantaneous bed shear stress, τ, according to $q \propto \tau^n$. In the field, bed shear stress is usually estimated from the free-stream flow velocity through use of some type of quadratic stress law, i.e., $\tau \propto C_f u^2$, where C_f is a friction or drag coefficient that varies significantly, $0{,}001 < C_f < 0{,}054$, from author to author. A common finding is that C_f differs between uprush and backwash: Cox *et al.* [26] and Conley and Griffin [27], for example, present time-averaged uprush coefficients, C_{fu}, that are typically greater than the time-averaged backwash coefficients, C_{fb}. Enhanced bed shear stress during the uprush has been attributed to several processes including in/exfiltration effects, flow accelerations and bore turbulence [16].

Barnes *et al.* [15], addresses these issues by providing the first comprehensive data set of direct stress measurements obtained using a shear plate within the swash zone. The data show rapid temporal variation of the bed shear stress through the leading edge of the uprush, which is typically two-four times greater than the backwash shear stresses at corresponding flow velocity (see Figure 4.19). Swash zone friction coefficients were back-calculated using a combination of measured and modelled flow velocities, as can be seen in the figure above. Despite the temporal variation of C_f, some success can be gained from the estimation of a different C_f for uprush and backwash. Figure 4.19 shows measured and predicted τ_0 in the swash zone, with the uprush and backwash C_f have been selected to best-fit the results: $C_f = 0{,}015$ for uprush, and $C_f = 0{,}009$ for backwash.

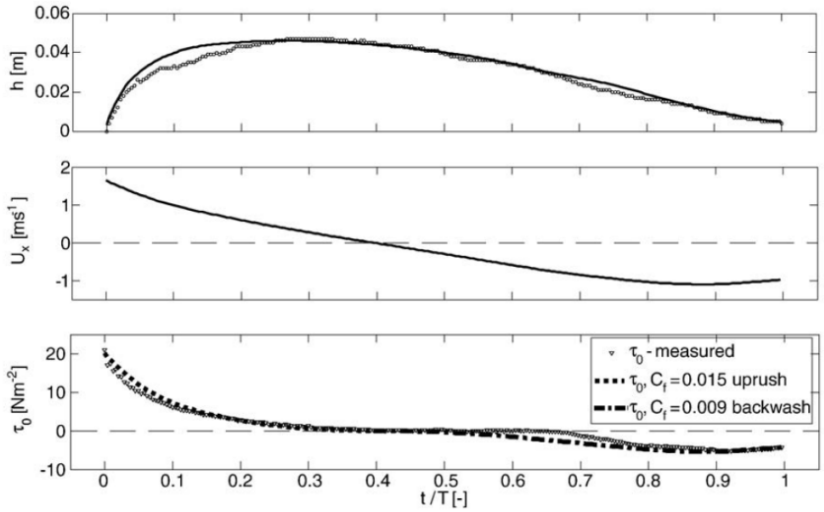

Figure 4.19 Measured and modelled depth and horizontal swash velocity, U_x,.measured bed shear stress, τ_0, and calculated bed shear stress with constant C_f [15].

Sediment transport using the full ADV data

When considering the complete flow-velocity wave data acquired with the ADV, it is possible to determine the sediment transport associated with it using the Bailard formulation. The following figures (Figure 4.20) present some exemplificative graphs of the calculated cross-shore sediment transport, q, for four different waves using the same formulation. Different values for the uprush and backwash friction coefficients, C_f, as described above were considered.

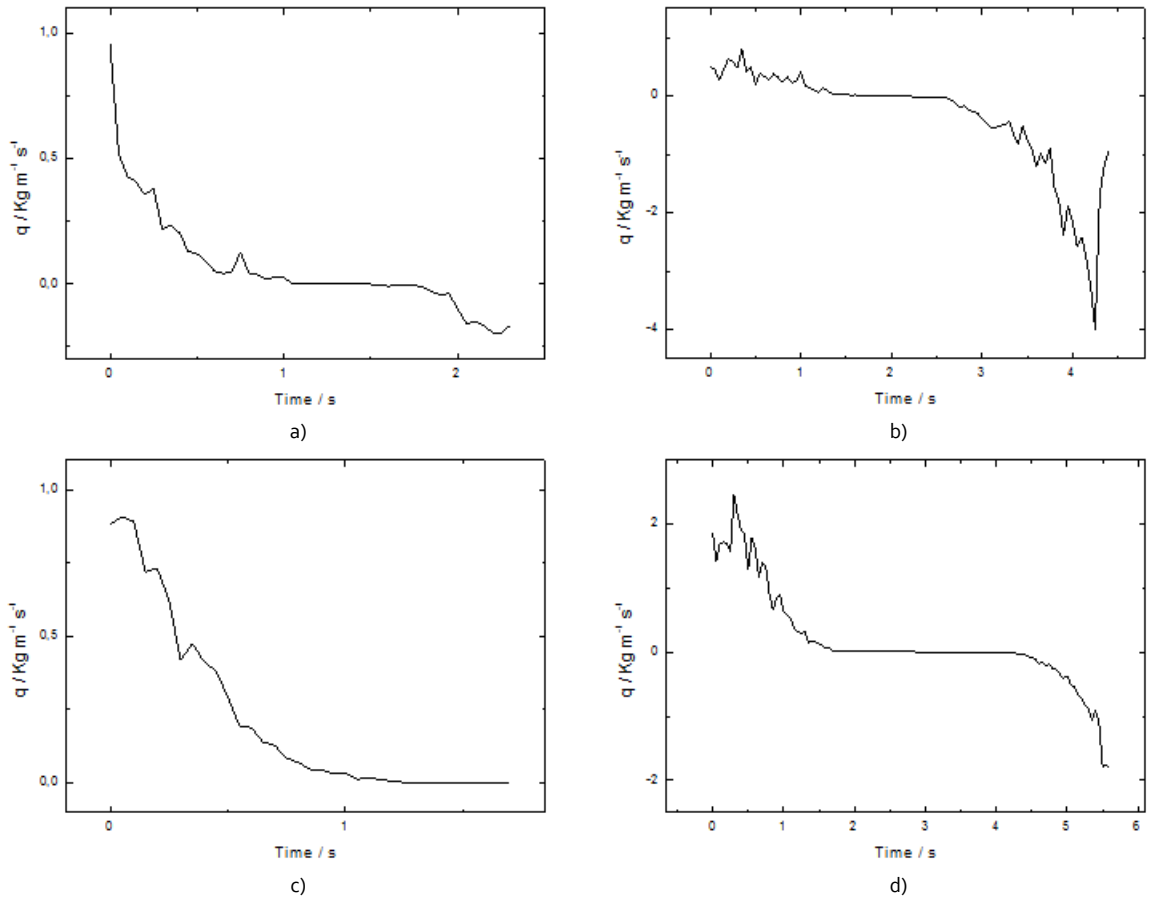

Figure 4.20 Examples of instantaneous cross-shore sediment transport for four different waves in the record.

It is possible to observe a plenty diversity of curves for the value q. Thus, some of the waves have associated a positive net sediment transport (accrection) as for the a) and c) graphs; graph b) have associated a negative net sediment transpost (erosion); and also others don't have a significant sediment transport associated because the positive and negative parts of the graph are approximetely equal, as can be seen in graph d). Notice that the positive values for q are associated with the uprush events, and, on the other side, the negative q values are related with the backwash events.

So, taking in account the complete wave flow-velocity data and consequently the diversity of curves for the value q, the net sediment transport rate across the section where the ADV was placed was estimated, and therefore the volumetric sand changes inland of that point. That was around 0,05 m^2 per meter of beach width, or 134 Kg per meter of beach width, which corresponds to an increase of the topographic level in the order of 4,5 cm in the considered profile along the 3 meters after the ADV point.

Sediment transport using the equivalent wave

Now, considering the equivalent wave for the whole tidal cycle, already obtained and shown in Figure 4.16, it arises that the respective graph of the cross-shore sediment transport, q, is the represented in the following figure (Figure 4.24).

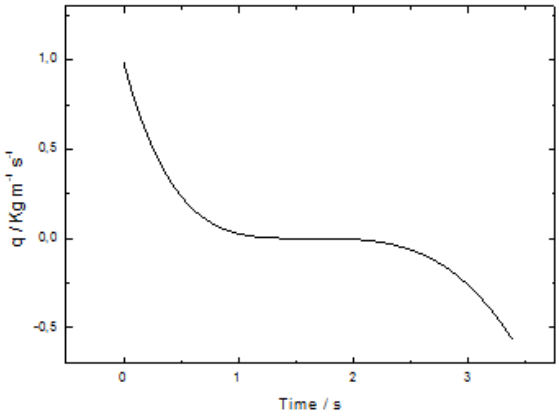

Figure 4.24 Cross-shore sediment transport for the equivalent wave.

It is evident that the transport associated with the equivalent wave is slightly positive, since the sediment transport during the uprush event is somewhat higher than the sediment transport during the backwash. As the number of waves collected in the complete ADV270102 file was 462, the volumetric sand changes can be computed multiplying the value associated with a single equivalent wave with the total number of waves observed. The result achieved is an accretion of around 42 Kg per meter of beach width (0,016 m^2 per meter of beach width), which in its turn corresponds to an increase of about 1,5 cm in the sand level.

4.6 Conclusions and final considerations

With the data gathered with the ADV during the campaign at Ancão beach, it was possible to estimate the sand level changes during one tide occurring in a region next to the device by two different ways: using the complete wave flow-velocity series; and using an equivalent wave. An important result achieved was that both of the used methods are in congruence. In other words, both are predicting a value of the same order of magnitude which is most important result at all, as well as both are predicting that accretion should happen. Besides all this and to confirm the last results, they are also in agreement with the topographic data acquired during low tides between the high tide in question.

Despite the wave characteristics are practically symmetrical and skewness and kurtosis have a negative value, the estimated transport has a positive value. The reason for this can be due to have been considered different friction coefficients, C_f, for uprush and backwash processes. This implies, apparently, that the sand transport phenomena taking place in the swash zone isn't determined by the cross shore velocity asymmetry as expected, but by other processes already covered indirectly in the different friction coefficients values. Nevertheless, the values obtained are so small that nothing can be said about the numerical values themselves. This arose from the fact that the waves that were breaking in that moment were small amplitude waves, and consequently, a very low hydromorphodynamics was observed during the tidal cycle. Furthermore, the sand level changes associated with hypothetical wind processes, or just human

activity, are significant when compared with the range of values achieved, as well as the errors related with the topographic survey measurements which is in the order of few centimeters.

It is important to say that some approximations were done during the entire process. For example, just cross-shore flow velocities (U_x) were considered to determine the volumetric sand transport by means of Bailard formulation; or just regular waves, as the wave shown in Figure 4.5, were considered to determine the important parameters that define the equivalent wave. These approximations and the use of an equivalent wave for one tide, however, didn't seem to influence the final results and so its use was suitable to solve the problem.

Finally, and although the results achieved weren't significant, the procedure to analyse future ADV data is completely done and controlled, as so as the procedures to determine sediment transport.

Chapter 5: Fiber Bragg gratings in optical fibers

Fiber optic sensor has been one of the most benefited technology of the remarkable developments that were being achieved by optoelectronics and fiber optic communications industries. The ability to carry gigabits of information at the speed of light increased the research potential in optical fibers [28]. Simultaneously, the improvements and cost reductions in optoelectronic components leaded to the appearance of new product areas [29]. Soon, it was discovered that with the low material loss, combined with changes in phase, intensity, and wavelength, resulting from outside perturbations on the fiber, could be used to sense those perturbations. Hence fiber optic sensing was born [30].

In parallel with these progresses, the sensor applications have often been driven by the needs and subsequent mass production of components to bear these industries. The requirement of a high volume of fiber for the telecommunications industry has brought down substantially the material cost for the fiber sensor, while the performance of the fiber was improving considerably over the years [31]. As a result, the ability of fiber optic sensors to replace traditional sensors for rotation, acceleration, electric and magnetic field measurement, temperature, pressure, acoustics, vibration, linear and angular position, strain, humidity, viscosity, chemical measurements has been exploited [30, 32-41].

In the early days of fiber optic sensor technology, the commercially successful sensors were directly targeted at markets where existing sensor technology was nonexistent or insignificant. These kinds of sensors were and are excellent candidates for monitoring environmental changes as they offer many advantages over conventional electronic ones. These inherent advantages of the optical sensors are: (i) immunity to electromagnetic interference, radio frequency interference and inability to conduct electric current; (ii) ability to be lightweight, with a very small size, passive, low-power consumption; (iii) high sensitivity; (iv) multiplexing capability to form sensing networks, remote sensing capability; and (v) environmental ruggedness. These advantages were heavily used to counterbalance their major disadvantages of high cost and unfamiliarity of the end-user [30, 40].

During the present thesis chapter will be briefly described the main features of optical fibers with Bragg gratings, as well as their fabrication techniques and principle of operation. Some pressure sensors based on Bragg gratings are also presented.

5.1 Photosensivity in optical fibers

Photosensitivity, defined as the capacity to have the refractive index of a medium permanently changed by the modification of its physical or chemical properties through intense light exposition [42], is a complex phenomenon due to the diversity of both parameters and effects that are observed. The different physical parameters changed during the light exposition process aren't only the refraction index, but can be also absorption, tension state, birefringence, coefficient of thermal expansion, or density. Furthermore, fiber composition, or even light source wavelength, are different parameters that can have a considerable influence on the photosensitive properties of the fiber [43].

The photosensitivity in silica optical fiber was first discovered in 1978 by Kenneth Hill *et al.* in glass silica fibers at the Communication Research Centre (CRC) in Canada [44]. However, pioneering work at the United Technology Research Centre, which is regarded as a milestone for

in-fiber Bragg grating (FBG) sensors, was published eleven years later by Meltz *et al.* [45]. This side-writing technique creates a Bragg grating directly in the fiber core using a holographic interferometer illuminated with a coherent ultraviolet source. Versatility in the fabrication of FBGs has been gained from the fact that the Bragg wavelength is independent of the used writing laser [42].

Hence, photosensitivity plays a key role in fiber Bragg gratings and several techniques have been developed to improve the effect. In most common optical fibers, the change of refractive index due to radiation exposition, at 244 nm, exhibits typically values of 1×10^{-5}, which is low for most of the applications. Thus, special photosensitization techniques such as: (a) doping with Germanium, Boron, Tin, rare-earth elements (co-doping), or (b) Hydrogen loading and densification (hydrogenation), all leading to increase the photosensitivity, became progressively studied and improved by laboratories. The state-of-the-art techniques now reach refractive index changes around 10^{-3} or 10^{-2} [43, 46].

Besides this, models are being developed with the objective to understand the photosensivity phenomenon, and trying to reach an agreement between them and experimental evidences as well. There are several different models with different concepts and mechanisms, like: i) color-center model, developed when researchers believed that photosensivity only occurred in the presence of Germanium; ii) the electron charge migration model, based on the appearance of a periodic electric field by photoexcitation of fiber defects; iii) stress-relief model, which consider that a decrease of thermoelastic stresses inside the fiber core causes a modification on the refraction index; and iv) compaction/densification model, which assert the possibility of laser radiation prompt variations on glass matrix density, and, consequently, causing variations in the refractive index. Although quite a lot of experiments corroborate some proposed models presented previously, there still exist some contradictory results in what change of refraction index values concerns. This indicates that all different mechanisms prevail in optical fibers, and the relative importance of each contribution depends on the type of optical fiber and photosensitization process used [43, 47].

5.2 Fabrication techniques of fiber Bragg grating

The fabrication techniques are crucial to obtain high quality and low cost in the FBG sensor technology. An ideal FBG fabrication technique should have the following features: i) flexibility (reflectivities and central wavelengths of produced FBG's should be selectable); ii) economical mass production capability (mass production of FBG's at high speed and low cost); iii) good physical and optical qualities (the mechanical strength of a produced FBG should not be degraded significantly after production, also a narrow spectral linewidth and a low excess loss are required); iv) good repeatability (repeatabilities of a FBG should be good enough in order to make FBG's standard devices under the condition of mass production and interchangeable without calibration) [48].

The first fabrication method for fiber Bragg gratings, already mentioned previously, was achieved by Kenneth Hill *et al.* [44] by interfering light that propagated in a forward direction along an optical fiber with the light reflected from the fiber end, as can be seen in Figure 5.1 (left). This method is known as the internal writing technique, and the gratings were referred to as Hill gratings. These gratings suffer from the limitation that the reflected light wavelength is the same of the wavelength at which they were written [49, 50].

The externally written Bragg gratings, which corresponds to an interferometric writing approach for inscribing Bragg gratings in photosensitive fibers, was first demonstrated by Meltz. In this case (see Figure 5.1 - right), the light from an UV source is split into two beams that are brought together so that they intersect at an angle θ, forming an interference pattern focused on the optical fiber core. Unlike the internal writing technique, the fiber core is irradiated from the side, giving rise to its name. The technique works because the fiber cladding is transparent to the UV light, whereas the core absorbs the light strongly. Most important is that FBG's can have a response in the spectral regions that are of interest for fiber optic communication and optical sensing, since the availability of optical sources is high [49, 50].

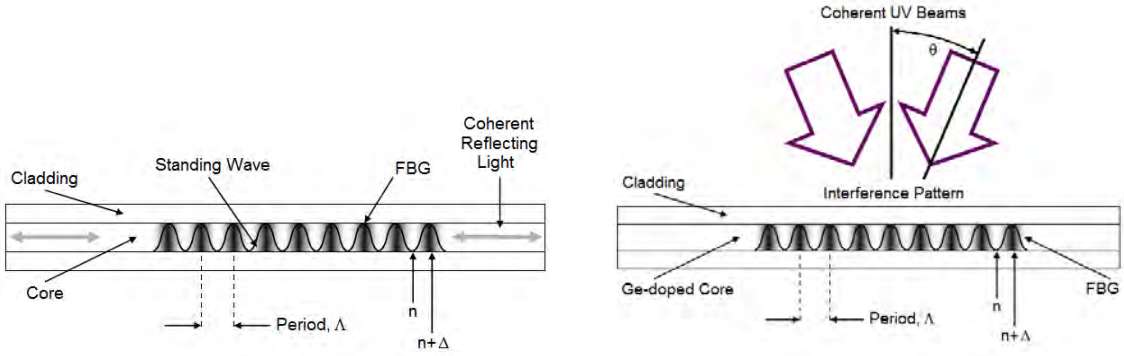

Figure 5.1 Left: grating written with standing wave inside; right: side-written Bragg grating with an interference pattern.

Today, both of these methods have been surpassed/enhanced by the use of the phase mask, another technique for FBG fabrication [51, 52]. The phase mask is a planar slide of silica glass or similar structure which is transparent to UV light. A periodic structure with the appropriate periodicity is etched onto the glass slide using photolithography. As shown in Figure 5.2, the optical fiber is placed close to the phase mask while the UV light is diffracted by the periodic structure of the phase mask, creating the desired grating structure in the fiber core. The periodic structure created in the fiber is one half of the spacing of the periodic structure in the phase mask. Besides this, the periodicity of the FBG is independent of the UV light source wavelength, being this selected on the absorbance spectra of the doped optical fiber core - thereby maximizing the source's efficiency in writing gratings.

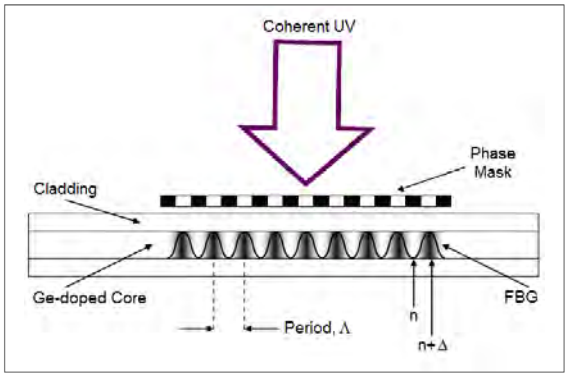

Figure 5.2 Side written Bragg grating with phase mask.

Use of phase masks made possible a lower cost and also higher precision Bragg gratings by simplifying the manufacturing process. In addition, this technique made possible the ability to automate the grating writing, and to write multiple gratings on a fiber simultaneously. It allowed as well the efficient writing of other types of gratings such as chirped gratings, which have non-constant periodicities for a wider spectral response (useful in the manufacturing of dispersion compensators) [49, 50].

5.3 Fiber Bragg grating operation

The operation principle of a fiber Bragg grating can be explained using the reflection principle of electromagnetic waves. When an EM wave passes through an interface between two dielectric mediums, with different refractive indexes, occurs a partial reflection known as Fresnel reflection. When the light is at normal incidence to the interface ($\theta_i = \theta_t = 0$), the reflection coefficient is given by [50],

$$R = R_S = R_P = \left(\frac{n_1 - n_2}{n_1 + n_2}\right)^2 \tag{5.1}$$

where n_1 and n_2 are the refractive indexes of the two mediums. Thus, in the presence of a small refractive index change, δn, also exists a small reflection. For example, $\delta n \approx 10^{-4}$ corresponds to $R \approx 10^{-9}$. However, in a FBG there are thousands of Fresnel reflections, i.e., can occur a strong reflection whenever all the reflections are coupled, as illustrated in Figure 5.3 [51]. So, as the signal moves along the fiber and encounters the interface between regions with different refractive indexes, a small amount is reflected at each boundary. When the period of the grating and the wavelength of the light are related by equation 5.2, there is positive reinforcement and power is coupled from the forward direction to the backward direction. Light of other wavelengths encounters interferences out of phase, therefore cannot propagate.

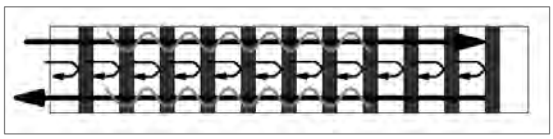

Figure 5.3 Principle of operation for a FBG.

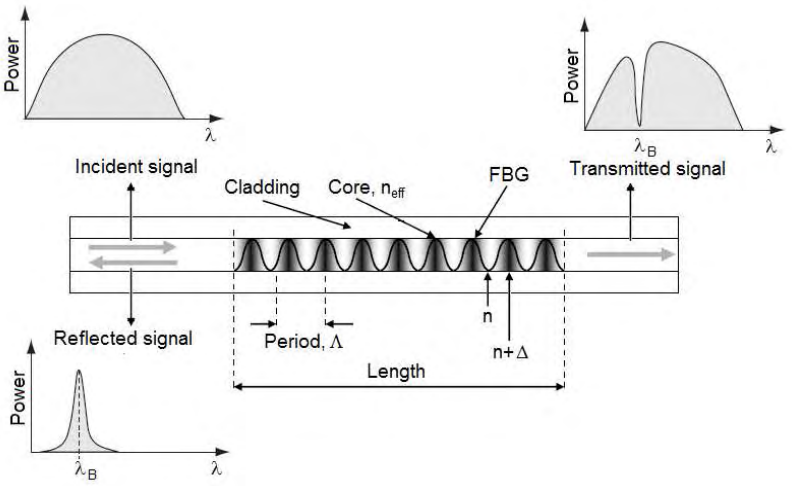

Figure 5.4 Schematic diagram of structure and spectral response of fiber Bragg grating.

Light is reflected in the grating when the wavelength (known as the Bragg wavelength, λ_B) satisfies the Bragg condition,

$$\lambda_B = 2n_{eff}\Lambda \tag{5.2}$$

where n_{eff} is the effective refractive index of the guided mode in the fiber, and Λ is the period of the refractive index modulation described by,

$$n(z) = n_{co} + \delta n[1 + \cos(2\pi z/\Lambda)] \tag{5.3}$$

where n_{co} is the unexposed core refractive index and δn is the amplitude of the photo-induced index. This effect is seen above in Figure 5.4.

5.4 Characteristics of fiber Bragg gratings

The most important characteristics of any FBG are, (a) the central wavelength, λ_B, which is the wavelength at the centre of the grating's reflection band; (b) the bandwidth, that is the width of the reflection band and specifies the range of wavelengths reflected; and (c) the reflectance peak, that is a measure of the proportion of incident light reflected at the central wavelength. These characteristics are determined by the basic parameters of the grating which are illustrated in Figure 5.4. These are: i) grating period, the distance between modulations of the refractive index in the grating; ii) grating length; and iii) "modulation depth" or refractive index contrast profile, the modulation depth may be different in different parts of the grating. The refractive index contrast profile describes any regular change imposed on the refractive index contrast (grating depth) over the grating length. The process of making regular changes in the grating strength in order to influence the characteristics of the grating is called "apodisation" (see [55, 56] and Chapter 5 from [47] for further information).

5.5 Sensing principles of fiber Bragg gratings

FBG sensors have been reported for measurements of strain, temperature, pressure, dynamic magnetic field, etc. As defined in equation 5.2, the Bragg wavelength is proportional to the grating period, Λ, and also to the effective index of refraction, n_{eff}. Therefore, any change of these parameters will cause a direct change in the Bragg wavelength, λ_B. This is the basis for the use of a Bragg grating as a sensor.

For the purpose of this thesis, only the sensitivity to externally applied mechanical and thermally perturbations are going to be considered, i.e., the sensors developed are just for strain and temperature sensing.

The strain field affects the response of an FBG directly, through the expansion or compression of the grating pitch, and through the strain-optic effect, that is, the strain-induced modification of the refractive index. The temperature sensitivity of an FBG occurs principally through the effect on the induced refractive index change and, on the thermal expansion coefficient of the fiber. Thus, the peak reflected wavelength shifts by an amount $\Delta\lambda_B$ in response to strain ε and temperature ΔT change, can be expressed by [57]

$$\Delta\lambda_{\mathrm{B}} = 2n_{eff}\Lambda\left(\left\{1-\left(\frac{n^2}{2}\right)[P_{12}-\nu(P_{11}+P_{12})]\right\}\varepsilon+\left[\alpha+\frac{\left(\frac{dn}{dT}\right)}{n}\right]\Delta T\right) \tag{5.4}$$

where P_{ij} coefficients are the Pockel's coefficients, υ is the Poisson's ratio, and α is the coefficient of thermal expansion of the fiber material. The factor $\{(n^2/2)[P_{12}-\nu(P_{11}+P_{12})]\} \equiv p_e$, the strain-optic coefficient, has the numerical value of $\approx 0{,}22$ and subsequently, the measured strain response at constant temperature is found to be

$$\frac{1}{\lambda_{\mathrm{B}}}\frac{\delta\lambda_{\mathrm{B}}}{\delta\varepsilon} = 0{,}78\times10^{-6}\mu\varepsilon^{-1}\,. \tag{5.5}$$

It should be reminded that the stretching limit applicable in an optical fiber corresponds to a strain, approximately, 3 %.

On the other hand, in silica fibers the thermal response is dominated by the factor $\{[dn/dT]/n\} \equiv \xi$, that is the thermo-optic coefficient, which accounts for ~95% of the observed shift. The normalized thermal responsivity at constant strain is

$$\frac{1}{\lambda_B}\frac{\delta\lambda_B}{\delta T} = 6{,}67 \times 10^{-6} K^{-1} . \quad (5.6)$$

For a wavelength of 1550 nm, and combining equation 5.2 with the strain and thermal responsivities expressed by 5.5 and 5.6, arises that the responsivities are $\sim 1{,}2 \text{ pm } \mu\varepsilon^{-1}$ and $\sim 10 \text{ pm } K^{-1}$, respectively.

Since a Bragg grating has a well-defined λ_B for each localized area of the Bragg structure, a number of sensors can be put on the same fiber core. Therefore, the gratings can be uniquely identified regardless of the distance between them along the fiber, allowing, for example, several number of strain sensors along one fiber with just one light source and detector. This configuration maximizes the multiplexing potential of Bragg gratings, and keeps system cost at a minimum as optoelectronics are much more expensive than FBG fiber.

5.7 Pressure sensors based on fiber Bragg gratings

Fiber Bragg gratings, as "on fiber" device, are ideal to integrate into optical fiber systems. There is a long list of existing and potential applications for FBGs which seems to grow every day (see Hill and Meltz [55], for exemple).

However, given the practical importance now attributed to pressure and temperature sensors, most of the work that is done today focuses on developing sensors of this type. So that, it's easy to find, in the various sources of information available, diverse types of pressure sensors which many of them are conceptually different. In the following table is represented the result of a bibliographic collection of pressure sensors based on this technology, with the corresponding operation principle of all of them, and also some peculiarity characteristics that they present.

Table 5.1 Pressure sensors based on fiber Bragg gratings; operation principle and description.

Concept	Description		Characteristic(s)	Ref.
Uniform strain of FBG	Force applied across the FBG	FBG embedded by a material that is under pressure	Simplicity	[59]
			Simplicity Polymer coating	[60]
	Force applied along the FBG	FBG attached to a cantilever beam	Temperature-compensated pressure measurement	[61]
		FBG housed in a glass bubble	Unusual concept	[62]
		FBG embedded in a polymer-filled metal cylinder with an opening on one side to enhance the pressure sensitivity	Simplicity	[63]
Single FBG with different applied strains in different locations	Force applied along the FBG	FBG bonded to the surface of the middle of a bilateral cantilever beam	Simultaneous measurement of force (or displacement) and temperature	[64]
	FBG embedded in a bar supported at the ends. The bar is deflected and, therefore, the FBG		Linear chirp	[65]
Based on a superstructure FBG	Force applied along the FBG			[66]

Chapter 6: Development of an optical pressure sensor using fiber Bragg gratings

The main focus of this chapter is to describe the development of an optical pressure sensor, its operation principle, the associated design decisions taken, and also the main features reached and added during the process. Beyond these, it is shown the thermal, humidity and mechanical characterization of the sensor, as well as its pressure response under real conditions. Future features will be discussed in the end, considering the results obtained.

6.1 Motivation and the operation principle

A novel optical fiber sensor for monitoring, in real time and remotely, the dynamic variations of the sea bed level in the nearshore was developed. This sensor is based on an optical fiber Bragg grating acting as a strain sensor, and has the purpose to determine the height of the sediment column that lies above a reference level, h_s. To perform its function, the device is initially buried at a known depth and then its behaviour over time is monitored. An illustration of these can be seen at right, in Figure 6.1.

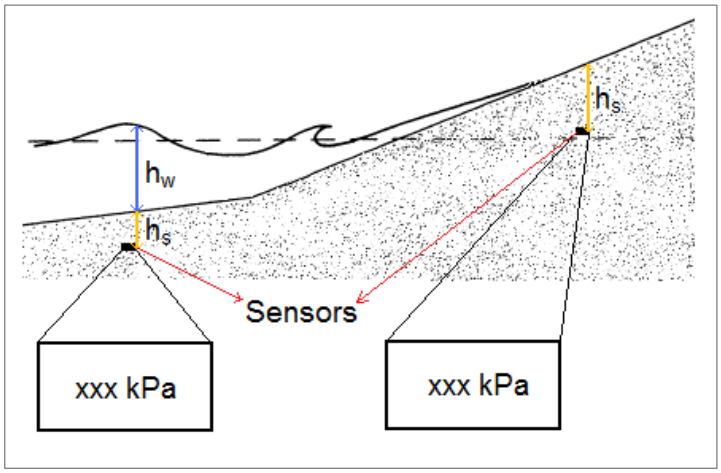

Figure 6.1 Schematic diagram of sensors at nearshore.

6.2 Material to transmit the stress (stress transmitter)

The first laboratorial approach to solve this problem was made using a concept already mentioned in Table 5.4, i.e., a FBG embedded in a polymer-filled metal cylinder proposed by Zhang *et al.* [63]. Thus, the initial idea was to implement a system similar to that. For that, it was necessary to find a material with the correct mechanical properties to act as a stress transmitter to the optical fiber. This material should have a Young modulus in the range of tens or few hundred MPa (like silicon rubber, which is $1{,}9 \times 10^2$ MPa [63]), and also should have the characteristic of strong adhesion to the optical fiber in order to transmit the total stress suffered. The Young modulus range of values desired was achieved during previous work done for the obtaining of the Bachelor degree (see [10]).

The materials tested to act as stress transmitter in the sensor were, (1) silicon rubber, (2) a polymer obtained by sol-gel process used at Chemistry Department, and (3) a polyurethane resin used in stickers(see the next section), shown in Figure 6.3. Their properties and advantages/ disadvantages for the usage as sensor are shown in Table 6.1. The Young modulus of the sol-gel polymer and the polyurethane resin shown in the same table, were achieved experimentally using a Shimadzu AGS-5kND mechanical test machine. The pressure versus displacement curve is presented in Figure 6.2.

Table 6.1 Materials tested to act as stress transmitter.

Material	Adhesion to optical fiber	Young Modulus	Advantages/Disadvantages
Silicon rubber	very bad	$1{,}9 \times 10^2$ MPa	Cheap and easily available. Too viscous and difficult to adapt to any kind of mold. Tested a mixture with an alcohol to become the silicone less viscous, but the resulting fluid didn't dry during several days.
Sol-gel polymer	not tested	$5{,}2 \times 10^3$ MPa *	Too brittle. Young Modulus too high.
Polyurethane resin	**strong**	$\mathbf{1{,}7 \times 10^2}$ **MPa** *	Excellent adhesion to the fiber. Quick curing process (maximum 2 days). Expensive compared with the silicone rubber. Available only by previous order.

* values obtained experimentally (see Figure 6.2)

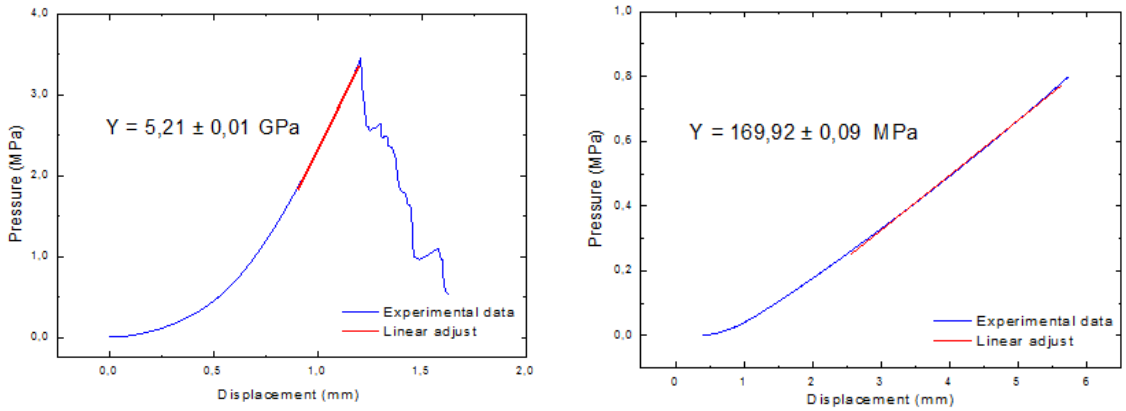

Figure 6.2 Pressure versus displacement curves of: Sol-gel polymer (left) and polyurethane resin (right).

Analyzing all information gathered in the table above, it's easy to see that the polymer chosen to be the pressure transducer, or stress transmitter, to the optical fiber pressure sensor was the polyurethane resin. Therefore, it will transfer the pressure on its top surface to the optical fiber. This was and still has been used in all sensor conceptions developed until today (see section 6.5).

6.3 Polyurethane resin

A polyurethane (IUPAC abbreviation PUR**)** are a large family of polymers all based in a chain of organic units joined by urethane (carbamate) links, with widely ranging properties and uses. These polymers are formed through step-growth polymerization by reacting a monomer containing at least two isocyanate functional groups with another monomer containing at least two hydrccoxyl (alcohol) groups in the presence of a catalyst. The process of polymerization, which is represented in Figure 6.4, is called "curing" and can takes from a few minutes to several hours. This process and the characteristics of hardened polyurethanes can be controlled through temperature, choice of resin and hardener compounds, solvents, and fillers added. It is also a highly exothermic reaction [67].

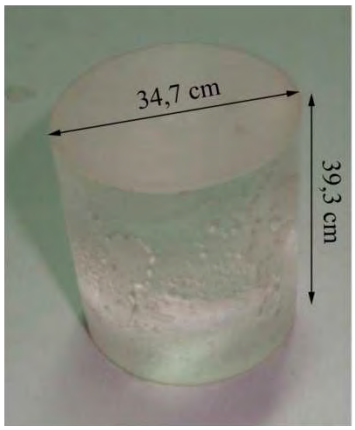

Figure 6.3 Cylinder of cured polyurethane resin used in mechanical tests.

Polyurethanes may be thermosetting or thermoplastic, rigid and hard or flexible and soft, solid or cellular with great property variances. As result of this attributes, they have found many

applications in different industries (e.g. electronics, aeronautics or astronautics) as protective coatings, fiber reinforced plastics, adhesives, foams, etc. Typical properties of polyurethane resins can be found in [68]. A photo of the polyurethane resin cylinder used for mechanical tests is presented in Figure 6.3. This resin was provided by Liquis Lens™ [69] and if bought in 400 ml cartridge, like used in this case, it has a price of £36,50 (around 42€).

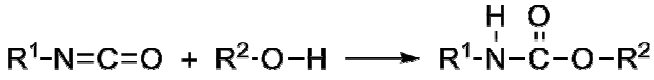

Figure 6.4 Generalized polyurethane reaction.

To guarantee that this polyurethane resin doesn't react with salt water, and consequently, can be used in nearshore regions, it was performed a mass test during ten days. This test consisted in immersing a previous weighed portion of the cured resin in sea water (was used the same cylinder that is presented in Figure 6.3), and measure regularly its mass during this time. It was seen that the mass tends to increase slightly, until these increases become more and more small. In the end were observed mass changes lower than 0,1 % which can be considered insignificant, although, one more test inside of sea water was performed. This is presented ahead in humidity characterization (section 6.5).

6.4 Sensor development progress

During the development of the sensor several decisions about its conception were taken, as well as also other changed/added features that are import to describe briefly. In the following pages are presented all the intermediate solutions until reaching the last proposed sensor, as also the most important problems and achievements reached for each of them. All of the conceptions are labelled with a version number, and for now on they will be used whenever needed.

It is important to control the temperature during the curing process of the polyurethane resin, to split the expected thermal effects of the mechanical effects, as both types can shift the Bragg wavelength of the FBG inside the resin. For that purpose, it was created a temperature sensor based on a FBG, with a Bragg wavelength different from the Bragg wavelength used for the sensor. Hence, the temperature was monitored with a FBG written in an optical fiber which was placed inside a double needle, as shown in Figure 6.5. The double needle protects the optical fiber from mechanical perturbations, and by this way the FBG is only sensitive to temperature variations [70]. As can be seen in Chapter 5, the thermal responsivity of this sensor is given by equation 5.6 which corresponds to ~10 pm K^{-1} at a wavelength of 1550 nm.

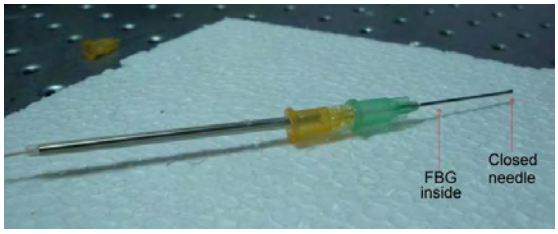

Figure 6.5 FBG temperature sensor used to control the temperature during the resin curing.

Finally, as the pressure is encoded in Bragg wavelength, it is indispensable to use a system capable of getting that optical information. All of optical data was, therefore, obtained using a SM125 Micron Optics interrogation system. This system has a resolution of 10 pm in the desired range of wavelengths, and a sampling rate of 1 Hz.

6.4.1 First attempt: polymer in a pot

This fiber optical sensor (version 1) was composed by a sensor house (pot) and a support, as shown on Figure 6.6. This configuration was based on previous articles reading, in particular the text by Zhang *et al.* [63]. The sensor house is made of polyvinyl chloride (PVC) filled with the polyurethane resin. The optical fiber in which the FBG is inscribed is vertically placed on support and a pre-tension is applied to the fiber (2 nm of the Bragg wavelength shift, approximately). After the resin cure process and the optical fiber be strongly adhered to the resin, the optical fiber termination (the part coming out of the resin through the top of the sensor) is removed by cutting the fiber. It's supposed that the pressure exerted at the top of the sensor contracts the resin in vertical direction, and so the optical fiber with the FBG (force applied along it). The existence of the PVC support has the purpose to let out the fiber cable, to block the fiber to curve too much, and also to hold it, since it was without coating protection. For this, it was used a support in metal (thin plate) where the optical fiber was glued with cyanoacrylate (super glue).

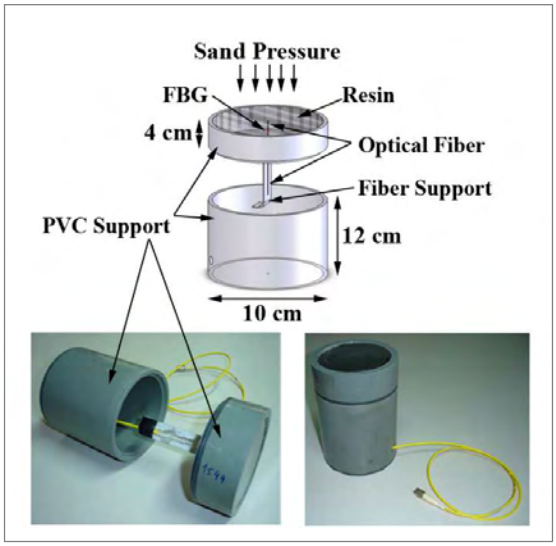

Figure 6.6 Schematic diagram and photo of sensor v.1.

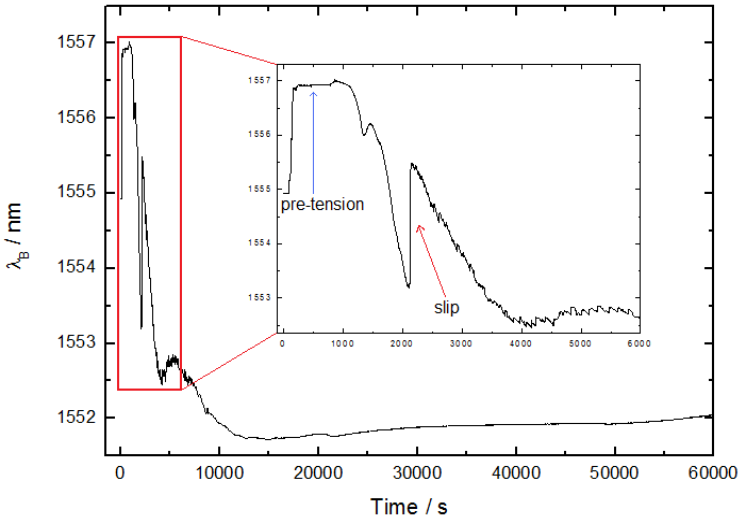

Figure 6.7 Bragg wavelength monitoring during the curing process of sensor v.1.

The curing process was monitored and the resulting graph is presented at Figure 6.7. Here, only one FBG was monitored, i.e., the FBG embedded in the resin and at the center of the pot, and therefore, no temperature was monitored. The reason for this is that it was the first successful attempt to create a sensor, and was unknown what to expect related to the behaviour of the resin along the process. The observation of the graph shows the imposed pre-tension of ~2 nm (blue arrow), and a first slip of about 2 nm (red arrow) with subsequent slips over time, which indicate that the fiber was sliding inside the resin. After ~30000 seconds the Bragg wavelength remained practically constant and it resulted in a shift of, approximately, 5 nm (from ~1557 nm to

~1552 nm), which implies that the resin contracts significantly during the cure despite all of the slips.

Finally, this first sensor version was tested under controlled and real conditions. The first were made using a setup like the one described in mechanical characterization (see section 6.5), nevertheless, they are not going to be presented or discussed ahead. On the other hand, the results obtained during the tests under real conditions were performed during the campaign at Ancão beach (see Chapter 4), and they will be briefly presented and discussed on section 6.6. Main achievements and problems related with sensor v.1 are presented in the next table.

Table 6.2 Achievements and problems related with sensor v.1.

Achievements:	**Problems:**
Noticed that the curing process implies a highly exothermic reaction, and so temperature must be monitored too.	It's very difficult to ensure that the optical fiber is perfectly in vertical position, whenever the PVC mold is filled with the resin.
Confirmed that the polyurethane resin acts as a stress transmitter to the optical fiber, in some extent.	The region of the optical fiber without protection was too fragile and unpractical, because the dried glue was too brittle.
Maybe the pre-tension may not be given, because of the strong resin's shrinkage, and subsequent slides of the optical fiber.	The curing process of the resin implies a strong shrinkage, and so undesirable, because the optical fiber slides inside the resin to recover a part of its initial stress state.
The sensor responds at visible pressure made by, e.g., hand or calibrated weights.	

6.4.2 Second attempt: polymer in a metal channel

The second attempt for the optical fiber sensor (v.2) is important since the operation principle was changed. Now, the fiber is in the horizontal position and the pressure acts transversally to it, i.e., the force is applied across the FBG. For that, the optical fiber was slightly tensioned and glued to two pieces of metal at both end-points inside a metal channel filled with the resin. At the tops were used two pieces of cardboard to ensure that the resin was molded to the right form. Notice also that the optical fiber termination without pigtail was removed by cutting the fiber. As a final result, when a hypothetical pressure is applied at the top of the resin, the resin expands for the directions non-constrained and consequently the FBG written in the optical fiber. A photo of the sensor and a scheme of its operation principle are presented in Figure 6.8.

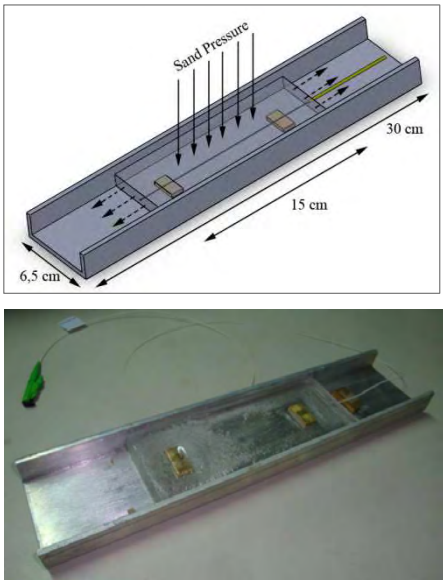

Figure 6.8 Schematic diagram and photo of sensor v.2.

In what curing process concerns, and analyzing the following graph in Figure 6.9, can be confirmed that this process is an exothermic reaction, with a temperature increase of, approximately, 70 °C from the room temperature (~0,7 nm of wavelength shift). It's also possible to conclude, at first, that the FBG embedded in the resin suffer an expansion due mainly to the temperature raise, and then suffer a retrenchment due to the resin contraction. So, in 3000 seconds (50 minutes) the embedded FBG is shifted from ~1553,5 nm to ~1552 nm, with the trend to go down further. The time scale is small compared to the graph in Figure 6.7, because the data plotted refers to a sensor that broke during the curing process.

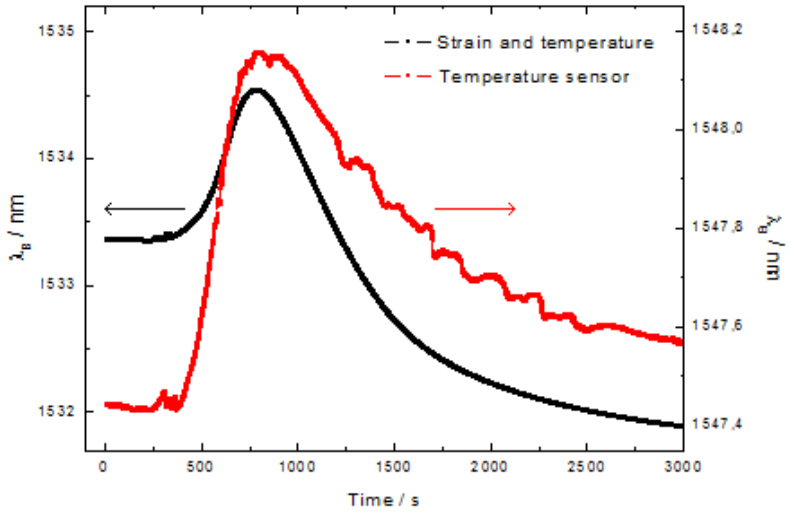

Figure 6.9 Monitoring of the temperature and FBG wavelengths during the curing process of sensor v.2.

With this configuration it was noticed that the behaviour of Bragg wavelength wasn't the expected, i.e., whenever a pressure is applied on top of the sensor, the optical fiber should stretch with the resin through the free direction on the metal channel, which doesn't occurs. For this reason, the Bragg wavelength should suffer a shift to higher wavelengths instead of the opposite. The reason for this may be the fact that the optical fiber is glued at two end-points, and so, when pressure is exerted over it, reacts as a deflected beam. To finish, this version wasn't tested and major features concerning to it are resumed in Table 6.3.

Table 6.3 Achievements and problems related with sensor v.2.

Achievements:	**Problems:**
Was monitored the curing process with a temperature FBG sensor, and confirmed that the process is a highly exothermic reaction. The resin adheres strongly to the metal channel. The pigtail was inserted inside the polyurethane resin, which became the connection more robust. The sensor responds also at visible pressure made by, e.g., hand or calibrated weights. Easier configuration and easier production than then previous version.	The cardboard adheres strongly to the polyurethane resin, and so it's difficult to remove it. Whenever the fiber is strained, the regions of it on top of the metal pieces become fragile, due to the fiber grazes over the metal. The procedure is difficult to repeat because the optical fiber breaks many times during the curing process. The behaviour of the sensor wasn't the expected.

6.4.3 Third attempt: polymer block

With these unsuccessful attempts, it was necessary to prospect another solution that overcomes the problems encountered. For that, it was thought about using a metal channel as a mold to a block of resin, where there are no constrains in any horizontal direction when a vertical force is applied on top of the block. With this, the pieces of metal were not anymore used, eliminating their effect on FBG response which was a problem.

Thus, the metal channel was quilted with duct tape and tested if it was easy to unmold the cured resin after the process. The pieces of cardboard at the tops of the channel were also quilted with the same duct tape, and drilled in the geometrical center to allow the fiber to pass through them. The principle of operation and conception was very similar of the preceding version, but now with any physical support for the resin. A photo and an operation principle scheme are showed in Figure 6.10.

At this time, and for all 3 sensors attempts to create this version of the sensor, the FBG inside the resin always broke during the curing process. The explanation for this can be given for the reason that now the polyurethane is not so strongly adhered to the mold, and the shrinkage is so significant that the optical fiber tends to broke; or else, for the reason that the temperature increase is too high and the recovery process is too aggressive for the optical fiber. A resume of major achievements and problems encountered are presented below.

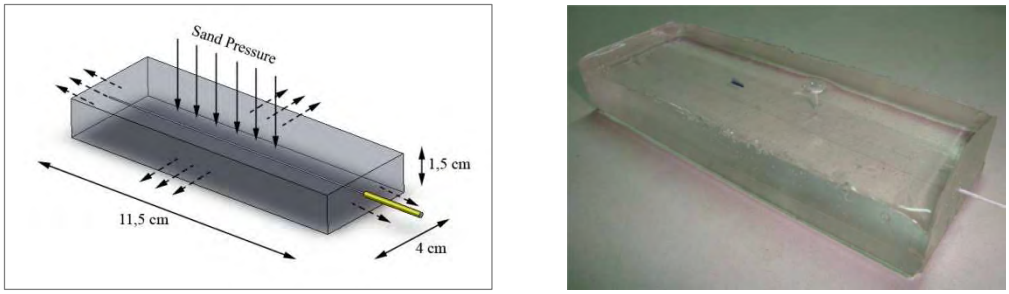

Figure 6.10 Schematic diagram and photo of sensor v.3.

Table 6.4 Achievements and problems related with sensor v.3.

Achievements:	**Problems:**
With duct tape is possible to mold a piece of resin inside a metal container, like a channel. The cardboard quilted with duct tape just adhere to the resin the sufficient, and is easily removed without major damage.	During the curing process the FBG embedded broke always. Unmold the resin block is risky, since there is strong probability to break the optical fiber.

6.4.4 Fourth attempt: polymer block resized

The solution for the previous problems passed by the resize of the polyurethane resin block, i.e., to reduce their length. For that, and knowing that cardboard quilted with duct tape is easily removed from the cured resin, were made cardboard boxes with the shape desirable for the block of the polymer. These boxes had a central hole on two opposite sides, where the optical fiber was placed and given a small pre-tension. After the curing process the cardboard was removed and the sensor obtained was the shown in Figure 6.11. With this procedure it was also avoided the unsafe and risky unmold of the resin inside the metal channel. Finally, a different a feature was tested which was the usage of a protective sleeve to protect the region where the fusion was made. The protective sleeve was inside and fixed to the polyurethane resin as can be seen in photo.

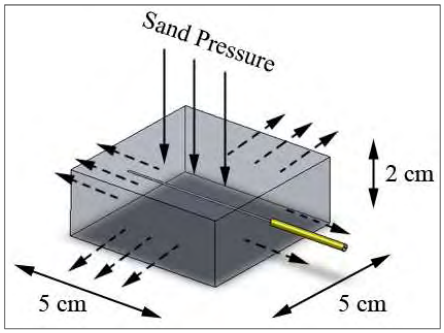

Figure 6.11 Schematic diagram and photo of sensor v.4.

After the curing process, the sensor v.4 seemed with a stable Bragg wavelength, which was the main achievement for this version (see Figure 6.12). This graph shows the response of the grating inside the resin (thermal effects plus strain effects), and it is clear that the optical fiber didn't suffer any slip during the curing course, becoming possible to characterize perfectly this cure process. Furthermore, it possible to infer that the FBG wavelength suffers a positive shift (~0,8 nm) in the initial

stage after resin deposition (~10 minutes), corroborating the graph in Figure 6.9. After this stage, the Bragg wavelength starts to decrease until it become stable 4,5 nm down of the initial value.

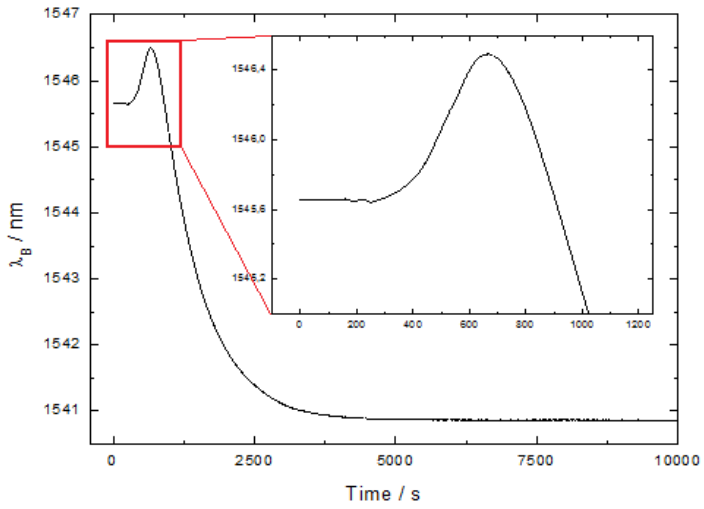

Figure 6.12 Monitoring of the wavelength of FBG embedded in the resin during the curing process of sensor v.4 (strain plus temperature).

Table 6.5 Achievements and problems related with sensor v.4.

Achievements:	**Problems:**
The FBG didn't break during the curing process. For the first time, it was reached a coherent plot of Bragg wavelength (embedded FBG) versus time. It's possible to mold a piece of resin inside a cardboard box quilted with duct tape. The sensor responds at visible pressure made by hand or calibrated weights. The range of values is satisfactory, meaning that this configuration can be also sensible for the desirable pressures applied under real conditions.	The manufacture process isn't the ideal, because the block of resin isn't as much regular as desired. The production procedure must be improved. Don't know the effect of the protective sleeve under real or controlled conditions. It was thought that the sensor itself was too small, and maybe a robust one may be achieved.

6.4.5 Fifth attempt: polymer cube

Although the last sensor version (v.4) was working in good conditions, it was tried another configuration very similar with it. The only difference was the height of the block, being now a block with cubic shape of side 5 cm (see Figure 6.13). This version and the earlier one were tested only under controlled conditions, and the results obtained were already presented [71].

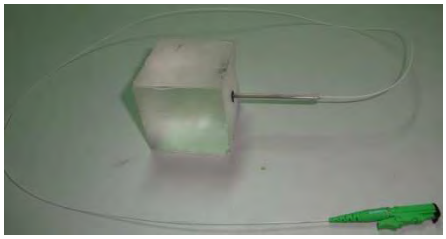

Figure 6.13 Photo of sensor v.5.

Analyzing the curing graph for this sensor, presented in Figure 6.14 is noted that the behaviour is similar to the previous one (version v.4). The difference is the stronger Bragg wavelength decrease and the innumerous slips of the optical fiber that occurred during the shrink of the resin (blue arrows). However, the sensor seemed operational and working as desirable.

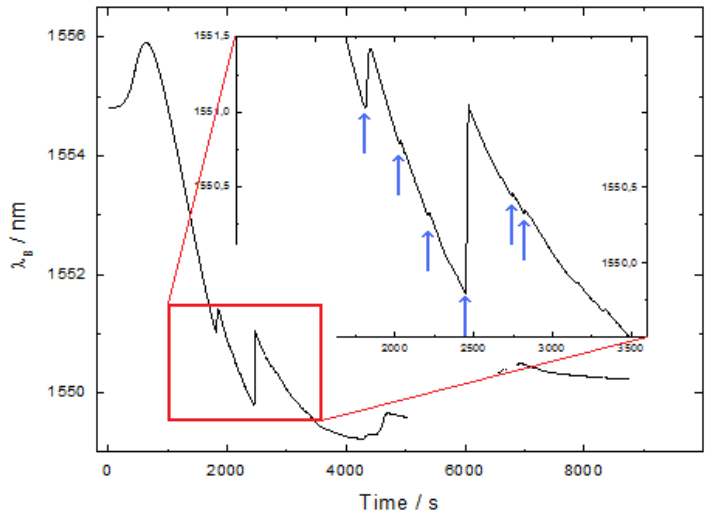

Figure 6.14 Monitoring of the wavelength of FBG embedded in the resin cube during the curing process of sensor v.5 (strain plus temperature).

Table 6.6 Achievements and problems related with sensor v.5.

Achievements:	**Problems:**
The sensor now is more robust. The sensor responds at visible pressure made by, hand or calibrated weights. The range of values is satisfactory, meaning that this configuration can be also sensible for the desirable pressures applied under real conditions.	The cure isn't coherent, because there is occurrence of some slips during it. Don't know the extension of this event. The manufacture process isn't the ideal, because the block of resin isn't as much regular as desired. The production procedure must be improved. Don't know the effect of the protective sleeve under real or controlled conditions.

6.4.6 Sixth attempt: final version to test repeatability fabrication

After five initial attempts it was reached a final version that could be tested under real conditions. This sensor is similar to version 4 but there were improvements, namely, in the production procedure (the sensor is a much more regular block). Also, the decision about the connection between the pigtail and the resin was that no sleeve protection is needed. The pigtail is therefore inserted a few millimeters inside the resin and bonded to it. Finally, all problems described in Tables 6.2-6 during the development process were solved, and a photo of the final is shown in Figure 6.15.

The plot of the cure course, with separated mechanical and thermal effects, is shown on Figure 6.16. As a result, during the exothermic reaction a temperature variation of ~40 °C was observed, simultaneously with an expansion of the resin. After the temperature reach its maximum value at ~530 seconds from the beginning of the curing process (t~200 s), it begins to decrease until room temperature and the resin starts to contract, getting to a minimum strain of ~-3300 με. After ~8000 seconds, the temperature has already reached a value of ~23 °C (room temperature) and a strong adhesion of the optical fiber to the resin was observed.

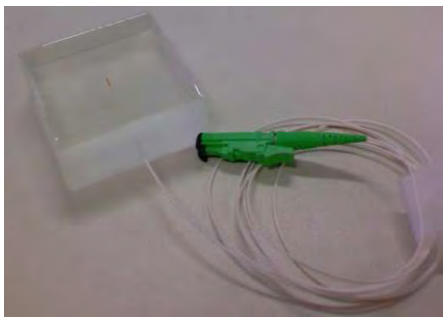

Figure 6.15 Photo of sensor v.5.

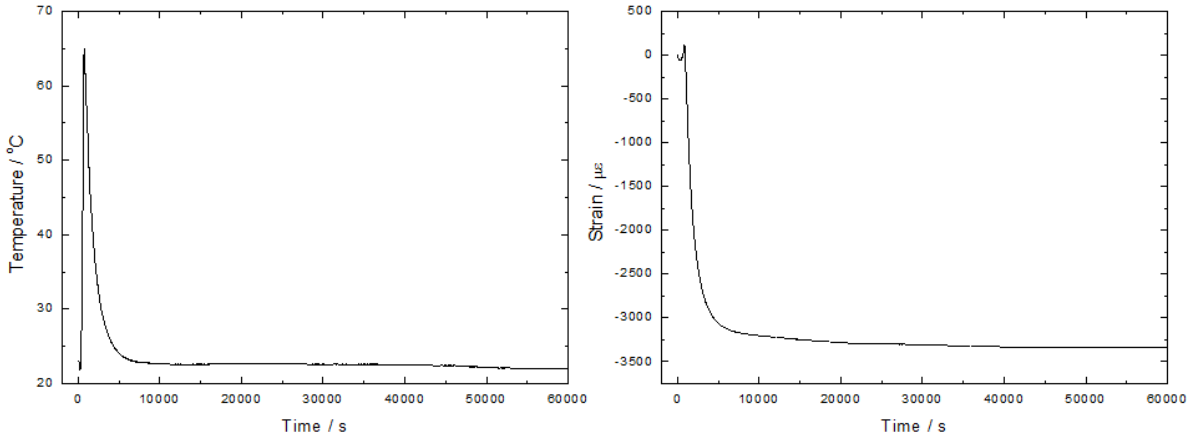

Figure 6.16 Curing process of sensor v.6. Left: temperature; right: strain.

As the production process was stable for this sensor, the same was repeated for five other sensors. All of them were very similar, as can be seen in Figure 6.17, and therefore it is possible to conclude that the production process of the sensor is reproducible.

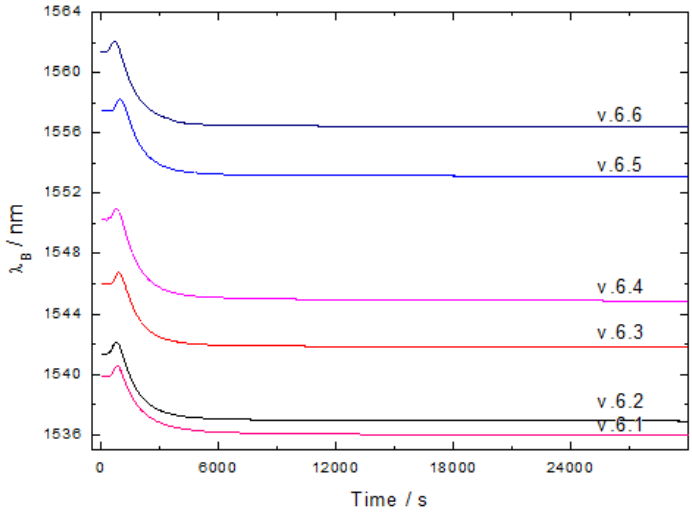

Figure 6.17 Curing process for all v.6 sensors (strain plus temperature).

Finally, the price associated with each sensor can be roughly evaluated (without shipping costs and logistics). Considering the resin price, the pigtail price (~20€) and the photosensitive fiber price (~80€ per meter), it gives an estimate of 36 € per sensor. It is import to note that the contribution of the resin price is practically negligible compared with the other costs.

6.5 Sensor characterization

The thermal and humidity response of the sensors v.6.2 and v.6.3 were achieved using an environmental chamber model CH340 *Angelantoni ACS*. The sensors were placed inside the chamber and, initially, keeping a constant temperature of 20 °C, the relative humidity (RH) was changed between 50 and 98 % at intervals of 10% with a two and half hours of transition time (note that the chamber couldn't reach 100% of RH). Afterwards, the RH was kept constant at 80%, and the temperature was changed between 10 °C and 40 °C at intervals of 5 °C during, as well, two and half hours. The response for both sensors is presented in Figure 6.18.

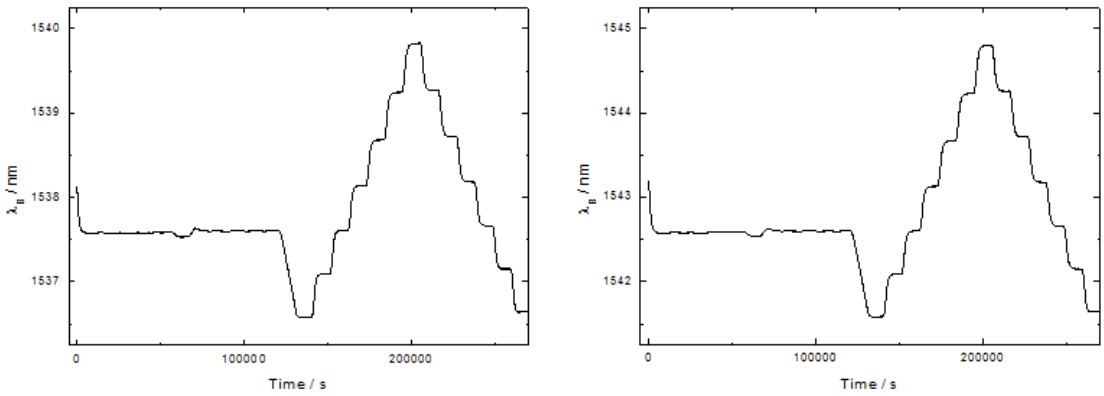

Figure 6.18 Bragg wavelength responses of optical sensors v.6 to different conditions of relative humidity and temperature. Left: sensor v.6.2; right: sensor v.6.3.

Examining the graphs above it is clear that the response of sensors for climate changes, namely relative humidity and temperature, is identical. It is worth mentioning that the humidity response of the sensors is practically null, with the changes of the Bragg wavelength being, nearly, less than 0,1 nm (further discussion is presented ahead in humidity characterization). On the other hand, temperature response is very consistent during temperature steps, namely comparing the ascending with the descending temperature steps which corresponds, approximately, to the same Bragg wavelength. The unique obvious difference relates with the different Bragg wavelengths for each sensor (there is a difference of 5 nm between them). Consequently, and taking also into account Figure 6.18, can be inferred that the sensors obtained are repeatable, i.e., the way of production is reliable and consistent. With this attribute it is also possible to say that the sensors produced are interchangeable without calibration, which is a fundamental characteristic of any sensor device.

Thermal characterization

Thermal characterization of the sensors was attained picking out the constant wavelength values achieved for each temperature step during the tests inside the environmental chamber presented above. Hence, the thermal sensitivity values were obtained by linear fit of the λ_B versus temperature points as can be seen in Figure 6.19. In Table 6.7 are exhibited the thermal sensitivity values for ascending and descending temperature steps for each sensor, such as the coefficient of determination, R^2, of the respective linear fit.

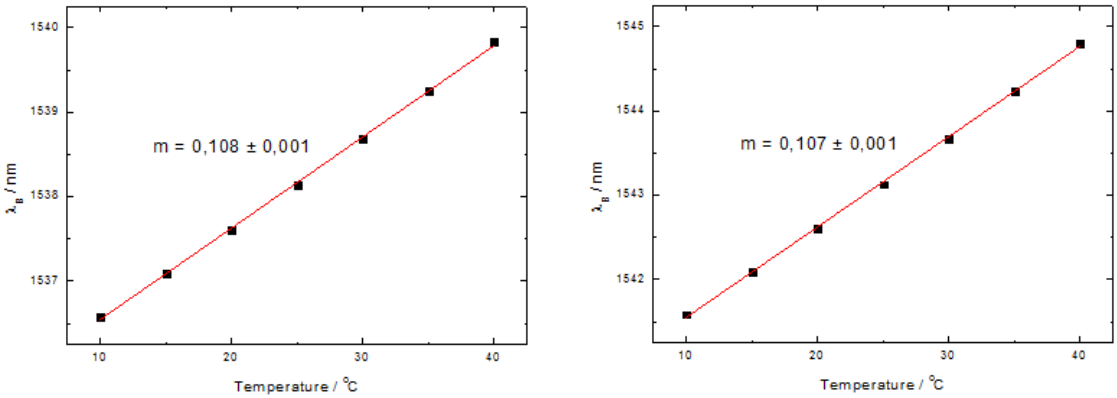

Figure 6.19 Thermal response of the optical sensors v.6. The dots represent experimental data and the red line the linear fit. Left: sensor v.6.2; right: sensor v.6.3.

Table 6.7 Thermal sensitivity values and R^2, for ascending and descending temperatures, for each sensor.

Sensor		Sensitivity / nm $^{o}C^{-1}$	R^2
v.6.1	asc.	0,108 ± 0,001	0,99928
	desc.	0,106 ± 0,001	0,99959
v.6.2	asc.	0,107 ± 0,001	0,99936
	desc.	0,105 ± 0,001	0,99967

Looking for the table above is corroborated what was said before. The thermal sensitivities achieved are very close from each other, around 0,108 nm $^{o}C^{-1}$, and the fitting have a good correlation coefficient ($R^2 > 0{,}999$). However, it is perceptible a small non-significant difference between sensitivities of ascending and descending temperature steps, that can be explained by the time given to Bragg wavelength stabilizes.

The stated highly dependence of the Bragg wavelength on temperature, justifies, when rigorous measurements are intended, the use of a temperature sensor near the location where the pressure sensor is deployed, in order to compensated this temperature dependence (see section 6.7).

Humidity characterization

As said earlier, there are no significant changes in the Bragg wavelength when the sensor is subjected to humidity changes. As can be perceived by Figure 6.20 the changes are larger while the chamber was set to have a value of 98% RH (red circle). These changes of about 0,1 nm maximum, can be related with temperature changes inside the chamber (around 1 ^{o}C, according to thermal sensitivity) during its attempt to maintain the same conditions of RH.

Though, and to eliminate the suggestion that the sensor is sensitive to water saturated environments, it was placed one of the sensors (v.6.2) inside a container with sea water. The Bragg wavelength sensor response was acquired during more than five days, in addition to a FBG temperature sensor as described in the beginning of section 6.4. Thermal compensation was made, and the Bragg wavelength response without thermal effects is shown below (Figure 6.21). Notice that at the start of data acquisition the sensor wasn't immersed in water yet. Consequently, it is easy to conclude that the sensor is insensible to the water immersion.

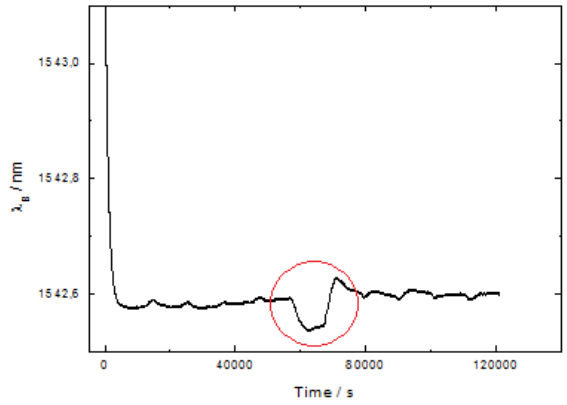

Figure 6.20 Humidity response of the optical sensors v.6.3.

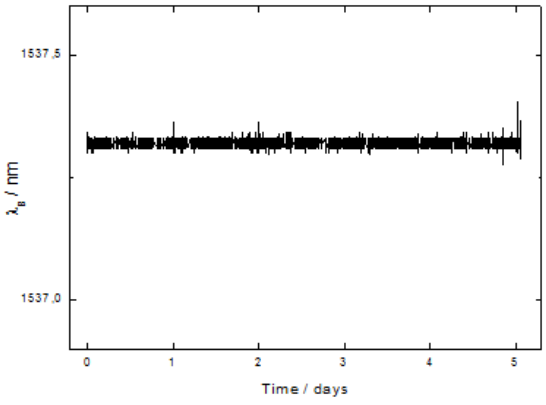

Figure 6.21 Response without thermal effects of the optical sensors v.6.2, whenever it is immersed in a container with sea water.

Mechanical characterization

Regarding the mechanical characterization of the sensors v.6, a Shimadzu AGS-5kND mechanical test machine was used, allowing the control of the applied pressure. The test was made for the sensor v.6.2. For that, it was placed inside a cylindrical PVC container with 15 cm radius, and then covered with 37 cm of sand. Finally, a PVC plate with 1 cm thickness and cut with the inner radius of the cylinder was put over the sand. So, whenever the mechanical test machine applies a controlled pressure over the plate, that amount of pressure is transferred trough the sand to the sensor, becoming possible to characterize the Bragg wavelength shift as function of the pressure applied (or the equivalent height of sand above, through equation 3.1).This principle is illustrated in Figure 6.22.

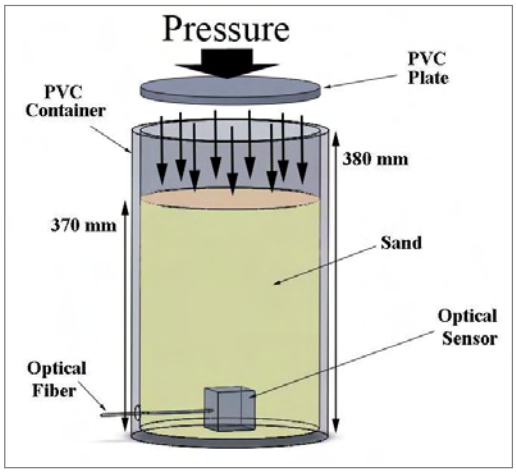

Figure 6.22 Mechanical characterization setup.

Sensitivity was obtained through the data showed in Figures 6.23 by linear fit to the experimental data of pressure as function of the Bragg wavelength. Also, and in order to verify the reproducibility of the results and the response time of the sensor, were applied cyclic pressure charges to it while its response was collected over time. This cyclic data is presented in Figure 6.24. It should be emphasized that the sensor must always present the same response to pressure, since it has to be reproducible.

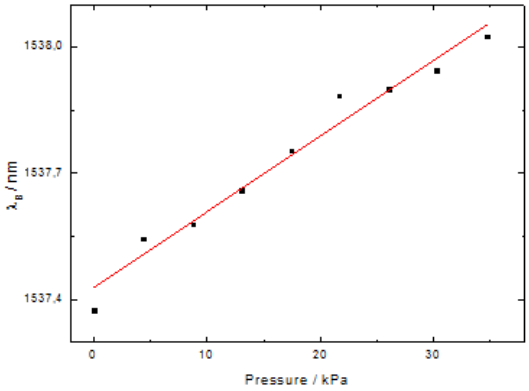

Figure 6.23 Bragg wavelength response for applied pressures on sensor v.6.2. The dots represent the experimental data and the red line the linear fit ($R^2 = 0{,}9678$).

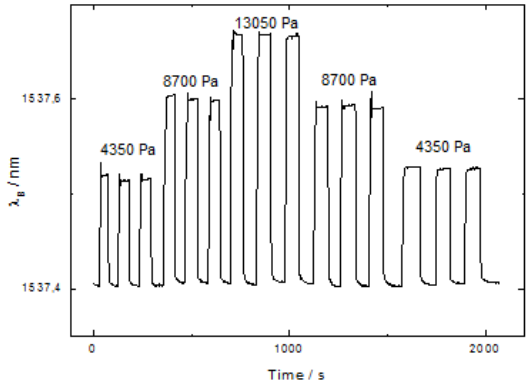

Figure 6.24 Response on cyclic charging over time for sensor v.6.2.

Sensitivity of 18 ± 1 pm kPa^{-1} was achieved for sensor v.6.2. Considering the equation 3.1 and sand density of 2650 kg m^{-3}, it comes that the sensitivity of the sensor can also be expressed by 0,47 ± 0,03 nm per meter of sand above the sensor. Taking into account the SM125 interrogation system, with a maximum error of 10 pm, it is possible to conclude that changes of about 2 cm on the sand level should be noticeable. Also, it is important to ensure that the tests made really simulate the real conditions encountered by a device buried on a sandy soil. Keeping in mind the theory presented in Chapter 3 (section 3.4), and admitting that the Bragg wavelength response to pressure is linear (Figure 6.23, with $R^2 = 0{,}9678$), can be assumed that the tests made for mechanical characterization were reliable.

On the other hand, the data presented on Figure 6.24 shows a good hysteresis of the resin and a reasonable response time. When subjected to pressures of around 13000 Pa the sensor take about 30 seconds to return to its original shape. Hence, the response time is adequate for measuring the slow variations of the sand bed as occurring in natural conditions; although, no signature of the surface waves with characteristic periods of 5-10 s should be noticed.

6.6 Sensor response under real conditions

From all of the versions presented only two were tested under real conditions: sensors v.1 and v.6. The sensor v.1 was tested in an early point of this work and therefore the results weren't the expected. On the other hand, the results attained in a beach soil with the sensor v.6 were satisfactory. Both two are going to be presented and discussed.

Optical fiber sensor v.1 was tested during the field campaign at Ancão beach for a period of approximately 36 hours (25-27 March 2009). It was deployed near the ADV and PT, which data was analysed previously in Chapter 4, with the purpose to compare and correlate all information gathered. However, it was not possible, since the sensor response wasn't the predicted. The sensor was deployed under 0,5 meters of sand at the beach swash zone, to protect it from external physical factors, such as being moved by currents. Therefore, its location was only covered with water in some space intervals.

Figure 6.25 presents the optical sensor data and the sea surface level. Systematic increase of the sensor response is observed when water arrives to sensor location during flood, probably denoting onshore sand transport associated with the observed wave mild conditions. However, the Bragg wavelength response wasn't the expected since it increases over time instead of decreasing. Notice that the first rising, observed at hour two, should not be considered because the sand above the sensor was compacting after the deployment of it.

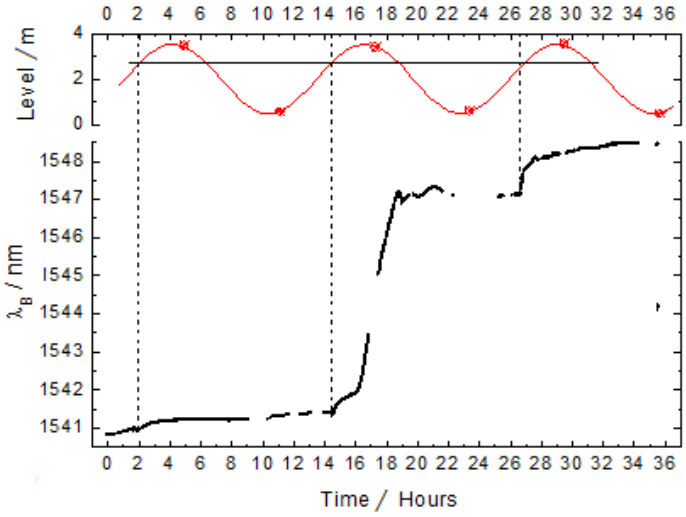

Figure 6.25 Optical sensor v.1 output and sea tide level. The dots represent the optical sensor data and the vertical dashed lines represent the times of water arrival to the sensor. The upper panel in the figure represents the sea surface level.

In the end, a shift of approximately 7,5 nm was observed, showing an exaggerated sensitivity, or that something happen to the optical fiber inside the resin. More data couldn't be accessed since the sensor broke during its recovery, showing that it wasn't a good option as a sensor. Finally, temperature changes of ~1 °C were measured using a thermometer at 0,2 meters depth. This temperature change was found to be small enough to be neglected, considering the total wavelength shift of the FBG. Hence, no more conclusions can be taken through the graph.

In what sensor v.6 test is concerned, it occurred in a sandy soil without being subjected to the waves influence, or even the swash processes. The reason is that the human and time resources to perform it are really significant, and these resources weren't available since Ancão campaign. Thence, it was only tested by burying it in a dry sand zone at a known depth, and acquiring the Bragg wavelength data for different column heights of sand above it. For that, the sensor was initially buried and covered with sand until the original bed level, and after, layers of known height of sand were being removed in a considerable area around the sensor position.

The response of the Bragg wavelength of the sensor v.6.3 for different sand heights is then presented in Figure 6.26. Besides, peak wavelengths of the spectrum were obtained by fitting Gaussian curves for each curve, resulting in the graph showed in Figure 6.27.

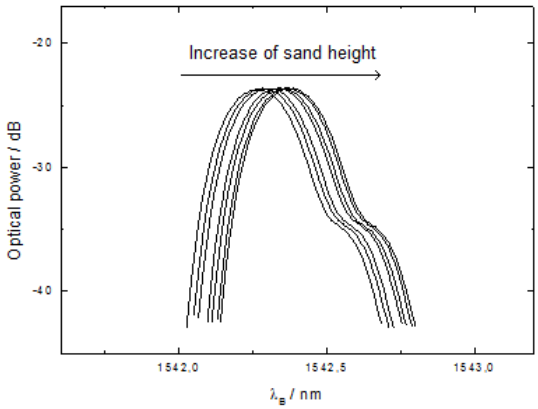

Figure 6.26 Bragg wavelength shit for different sand heights over sensor v.6.3.

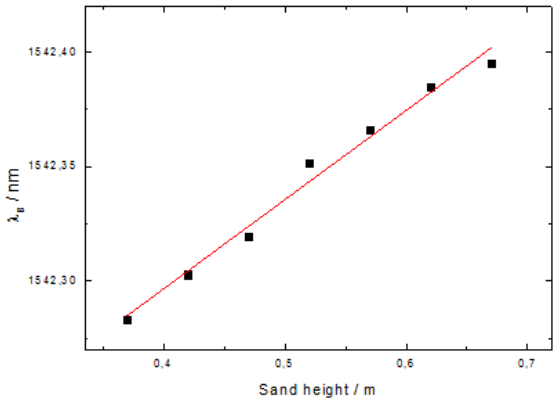

Figure 6.27 Bragg wavelength response for different sand heights over sensor v.6.3. The dots represent experimental data and the red line the linear fit ($R^2 = 0{,}9832$).

As can be seen in the previous figures, the sensor reacts whenever pressure is exerted on its top by the beach sand. This response is in accordance with the expected, i.e., an increase of the Bragg wavelength with the increase of sand height, and a linear relation ($R^2 = 0{,}9832$) as predicted by equation 3.1. Thus, the sensitivity achieved was 0,39 ± 0,02 nm per meter of sand above the sensor, which also corresponds to noticeable changes of about 2,5 cm on the sand level, taking into account the wavelength resolution of the optical interrogation system. Note that these results were obtained after some compression of the sand layers on top of the sensor; however, it is presumable that the compression achieved wasn't enough to be similar to the sand compression under natural conditions. So, the results obtained are simply qualitative.

Comparing these results with the others obtained with the mechanical characterization setup presented in Figure 6.22, infers that the sensitivity is lower when the sensor is under real conditions (0,39 ± 0,02 nm versus 0,47 ± 0,03 nm). This is completely expected since the sand compression achieved using a mechanical press is logically greater than the sand compression reached under natural conditions. Nevertheless, the sensitivities are comparable between them, which is, undoubtedly, a good result.

6.7 Final considerations and future improvements

This chapter showed the possible use of optical sensors for sea bed level changes monitorization which can be associated to the sand transport in surf zone. After describing the development process, it was finally achieved a low-cost, lightweight, small in size and self-referencing with a linear response sensor. Besides, this proposed sensor has an easy reproducible manufacturing process, which is a fundamental feature for any sensor.

The developed sensor is immune to humidity and water environments, although it shows a large sensitivity to temperature. For this reason, it is necessary to think about a way of monitor also the temperature of the environment where the sensor is deployed. Although it was not shown previously, some approaches to solve this problem were already made. Hence, a future improvement for the sensor can be the use of an optical fiber with two Bragg gratings written with different Bragg wavelengths, to compensate the temperature effect. One of the gratings would stay in the same central position embedded in the resin, and the new one would be outside the resin inside a needle, which, in turn, is inserted in the resin block. Notice, that it must be ensured that the needle is not filled with resin. In what sensors time both temperature and pressure response concerns, it is clear that they will not be a problem since the temperature and bed level changes are much slower than the "time constant" of the sensors response; however, the pressure due to waves shouldn't be perceptible. Finally, the polyurethane resin shows hysteresis when subjected to pressure or temperature changes.

More tests should be done using the sensors developed until now, namely field tests with high temporal scales in the range of weeks. For example, the sensors should be buried at well known places with a height graduation near to access the height of sand column. Afterwards, one or two weeks must pass on while the sand reaches its natural compaction and the sensor becomes part of sand system. Only after that time measures will take place, repeating it over some weeks. During these tests, or during a hypothetical campaign where the sensor is deployed nearshore, it is also fundamental to control the pore pressure in the same point where the sensor is. This problem isn't resolved yet; however, there are several devices which can perform pore pressure measures and can be used. To conclude, it is of considerable importance that the sensor stays with its top face always in a horizontal position, so that the measures will not be biased.

Chapter 7: Conclusions, recommendations for future work and potential applications

7.1 Conclusions and final considerations

Along this thesis were studied aspects related with two main subjects: hydromorphodynamics processes in the swash zone, and sensors based in optical fiber Bragg gratings. Initially, concepts of waves and soil mechanics in these specific regions were developed and described, as well as were analyzed a set of data acquired during a field campaign. Later, theoretical fundamentals of in-fibre Bragg gratings were introduced, and the description and presentation of the development of a sensor capable to perform measurements of the sand level in nearshore regions was made. The primordial purpose of this work was to relate directly the two different subjects comparing the acquired data from the common electronic devices (ADV's and PT's for wave flow velocities and water depth, respectively, and GPS for topographic measurements), with the response of developed optical fiber sensors deployed near the devices location during a field campaign performed at Ancão beach. However, it was impossible to complete this task, since the sensors used during the field campaign had shown an unexpected behaviour and frailty, as can be seen in Figure 6.25. Nevertheless, and in the end, acquired data from the ADV and correspondent PT were compared with the topographic measurements performed with a GPS verifying that they were in accordance; and, a novel sensor based on fibre Bragg gratings able to monitor sand levels was developed and perfectly characterized.

Comparison between estimated cross-shore sediment transport arising from the wave flow velocities measurements performed by an ADV and direct analysis of topographic measurements, were done in Chapter 4. Here, for exemplificative purposes, only one high tide data was treated, with waves being characterized for groups of 10 minutes concerning their most important parameters. Although it was verified small changes for different stages of the tide regarding these parameters, an equivalent characteristic wave of the tide was evaluated, which is shown in Figure 4.16.

Sediment transport inland to the ADV location was estimated resulting in: an accretion of 134 Kg per meter of beach width when considering the full ADV data (corresponding to an increase of the topographic level in the order of 4,5 cm); and an accretion of 42 Kg per meter of beach width when considering an equivalent wave for the whole tide (corresponding to an increase of about 1,5 cm in the sand level). On the other hand, topographic measurements showed an accretion of around 80 Kg per meter of beach width between low tides (changes in the order of 5 cm in some areas). These results are in accordance with each other; however, the stated sand level changes are so small that no further conclusions can be inferred since they are comparable with other factors, such as: wind, human presence in the local or errors associated with the topographic survey. Still, these results are valid since they are the expected due to the low hydrodynamics observed during that time, and they are in the same range. As a final point, it can be concluded that the Bailard formulation was convenient to solve the problem, as well as the use of different friction factors for uprush and backwash events.

Based on concepts introduced during the Chapter 5, the development and employment of an optical fiber Bragg grating sensor for the monitorization of sand level changes, such as the associated with sand transport, was exhibited and described on Chapter 6. The proposed sensor

is presented in Figure 6.15 and was accomplished after five sensor attempts. It has an estimated price of 36€, its fabrication process is a repeatable process, and presents the desirable robustness to be employed in sand beaches.

Humidity and thermal characterization were performed, showing that no humidity response is presented, even in extreme conditions like immersing the sensor inside a water container; although, a high and linear dependence on temperature was perceived, obtaining a thermal sensitivity of 0,108 nm $^{o}C^{-1}$ in the Bragg wavelength. This implies the need to temperature control when rigorous measurements are intended. Mechanical characterization of the sensor was also done, using either a setup configuration with a mechanical test machine, or burying the sensor several centimeters under beach soil. For the first case, it was achieved a sensitivity of 0,47 ± 0,03 nm in the Bragg wavelength per meter of sand above the sensor, which taking in account the resolution of the interrogation system used, corresponds to noticeable changes of about 2 cm on the sand level. On the other hand, and under real conditions, it was achieved a sensitivity of 0,39 ± 0,02 nm per meter of sand above the sensor corresponding to a difference of about 2,5 cm on the sand elevation above the sensor. Both responses showed a linear tendency, corroborating the assumptions made during Chapter 3 regarding soil mechanics ($R^2 = 0{,}9678$ and $R^2 = 0{,}9832$, respectively). The disagreement between the pressure sensitivities can be explained through the different sand compressions achieved in the different experiments which are, in turn, completely in agreement with the expected. However, any of these resolutions are better than the resolutions offered by the different systems presented in Chapter 2, which cause this technology to be suitable in the future.

7.2 Recommendations for future work and potential applications

As part of the evolution of science and technology, the work presented with this thesis cannot be considered closed or finished. Therefore, it is possible to enumerate some topics from where future work can be done.

Starting with the analysis process of the wave flow velocity data, it can be repeated and eventually improved with the intent to analyze the remainder data. An automatic script can also be developed with the purpose to analyze raw data prevenient from future field campaigns. During these new hypothetical campaigns, more ADV data should be acquired, aiming a more complete description of the area in study. For example, along-shore processes can be considered.

In what optical fiber sensor concerns and during future field campaigns (the next is expected to occur during the first semester of the next year), they should be tested during large time scales (several days and, if possible, weeks) and their results should be compared with frequent topographic surveys. The response of the sensors as an array of sensors acquiring at the same time should also be tested. Finally, new features should equip or assist the sensors, namely, temperature compensation, or a way to determine pore pressure at the site where they are deployed.

At last, and keeping in mind the features presented by the developed sensors, is rightful to propose different and potential applications where they can be used. For example, a sensitive optical fiber temperature sensor can be proposed; or else, position sensors can be developed based in the materials or the operation principle of the developed sensors.

References

[1] Whyte, W., and R. Paul, 1997. *Basic surveying (4th Edition)*. Buttherworth-Heinemann.

[2] Pascual, C., *et al.*, 2005. *Co-registration of lidar data by GPS and topographic measurements with sub-metric accuracy under dense forest canopy*. Universidad Rey Juan Carlos, Dpto. de Tecnología Química y Ambiental, Madrid, Spain.

[3] Martini, L., 2007. *Disciplina: Levantamentos Topográficos II - Topografia Aplicada aos Levantamentos Hidrográficos*. Universidade Federal do Paraná - Dep. de Geomática.

[4] Tedesco, A., C.P. Krueger, and J.A.S. Centeno, 2003. *Estimativa de profundidades utilizando imagens de alta resolução apoiadas por dados de levantamento batimétrico*. Univ. Federal do Paraná - Sector de Ciências da Terra, Curitiba, Brasil.

[5] Guenther, G., *et al.*, 2001. *Meeting the accuracy challenge in airborne LIDAR bathymetry*. EARSeL eProceedings, **1**: pp 1-27.

[6] Wozencraft, J.M., and W.J. Lillycrop, 2002. *Total shallow-water survey through airborne hydrography*. paper presented at Oceanology International 2002, Southampton Oceanography Center, London, UK.

[7] Irish, J.L., *et al.*, 2000. *Airborne LIDAR bathymetry: the SHOALS system*. PIANC Bulletin Vol. **103**: pp 43-53.

[8] Alt, C. von, 2003. *Autonomous underwater vehicles*. Wood's Hole Oceanographic Institute.

[9] Ramos P., *et al.*, 2000. *Outfall monitoring using autonomous underwater vehicles*. Conf. Proceedings of MWWD2000 Marine Waste Water Discharges International Conference, Genoa, Italy.

[10] Ferreira, L., 2008. *Simulação e sistemas de medição da evolução da topografia de fundo de uma praia*. Universidade de Aveiro, Dep. Física.

[11] Sorensen, R.M, 2006. *Basic Coastal Engineering (3rd Edition)*. Springer, USA.

[12] Austin, M. *et al.*, 2009. *Onshore sediment transport on a study beach under varied wave conditions: Flow velocity skewness, wave asymmetry or bed ventilation?*. Marine Geology, Vol. **259**: pp 86-101.

[13] Abreu, T, 2006. *Transporte de sedimentos em zonas costeiras – Dissertação para obtenção do grau de Mestre em Engenharia Civil,* Faculdade de Ciências e Tecnologia da Universidade de Coimbra, Departamento de Engenharia Civil.

[14] Brocchini, M. and Baldock T.E., 2008. *Recent advances in modelling swash zone dynamics: influence of surf-swash interaction on nearshore hydrodynamics and morphodynamics*. Reviews of Geophysics, Vol. **46**.

[15] Barnes, M.P. *et al.*, 2009. *Direct bed shear stress measurements in bore-driven swash*. Coastal Eng., Vol. **56**: pp 853-867.

[16] Masselink, G., and Russel P., 2006. *Flow velocities, sediment transport and morphological change in the swash zone of two contrasting beaches*. Marine Geology, Vol. **227**: pp 227-240.

[17] Harris, C.K., 2003. *Sediment transport processes in coastal environments – Lecture 1: Introduction and sediment properties*.

[18] Fernandes, M., 2006. *Mecânica dos Solos: Conceitos e princípios fundamentais (Vol.I)*. Universidade do Porto, FEUP Edições.

[19] Michallet, H. *et al.*, 2009. *Wave-induced pore pressure measurements near a coastal structure*. J. Geophys. Res., Vol. **114**.

[20] Breul, P. *et al.*, 2008. *On site characterisation and air content evaluation of coastal soils by image analysis to estimate liquefaction risk*. Canadian Geotechnical Journal, Vol. **45**, n. 12: pp 1723-1732.

[21] Janssen, H.A., 1895. *Experiments on grain pressures in silos*. Verein Deutscher Ingenieure, Zeitschrift.

[22] Mory, M., *Mécanique des fluides et ses applications pour la réaction chimique et les procédés de séparation mécanique*. Université de Pau et des Pays de l'Adour.

[23] B Bailard, J.A., 1981. *An energetic total load sediment transport model for a plane sloping beach*, J. Geophysical Res., Vol. **86**, C11: pp. 10938-10954.

[24] Masselink, G., *et al.*, 2008. *Cross-shore sediment transport and morphological response on a microtidal beach with intertidal bar morphology, Truc Vert, France*. Marine Geology, Vol. 251: pp 141-155.

[25] Emmanuel, I. *et al.*, 2009. *Sediment transport particular events and beach profile response*. 2009 ICS Proceedings, Portugal.

[26] Cox, D.T., *et al.*, 2000. *Bottom stress in the inner surf and swash zone*. Proceedings of 27th International Conference on Coastal Engineering, Vol. **ASCE**: pp 108-119.

[27] Conley, D.C., *et al.*, 2004. *Direct measurements of bed stress under swash in the field*. J. Geophys. Res. Vol. **109**, C03050.

[28] Selvarajan, A., S. Kar, and T. Srinivas, 2002. *Optical fiber communication: principles and systems*. Tata-MCGraw-Hill, India.

[29] Vinter, E.R., and Borge, 2002. *Optoelectronics*. Cambridge University Press, Cambridge, UK.

[30] Fidanboylu, K., and H.S. Efendioglu, 2009. *Fiber optic sensors and their application*. 5th International Advanced Technologies Symposium (IATS'09), May 13-15, Karabuk, Turkey.

[31] Elliot, J.C., and Barry, 2005. *Introduction to fiber optics (3rd Edition)*. Newnes-Elsevier, UK.

[32] Bjerkan, L., *et al.*, 1996. *Bragg grating sensor demodulation scheme using a semiconductor laser for measuring slamming forces of marine vehicle models*. Proc. 11th Int. Conf. on Optical Fibre Sensors, Sapporo, Japan, pp 236-9.

[33] Kersey, A.D., and M.J. Marrone, 1994. *Fibre Bragg high-magnetic-field probe*. Proc. 10th Int. Conf. on Optical Fibre Sensors, Glasgow, UK, pp 53-6.

[34] Morey, W.W., *et al.*, 1989. *Fibre optic Bragg grating sensors*. Proc. SPIE, Boston, USA, Vol. **1169**: pp 98-107.

[35] Morey, W.W., *et al.*, 1992. *Evaluation of a fibre Bragg grating hydrostatic pressure sensor*. Proc. 8th Int. Conf. on Optical Fibre Sensors, Monterey, USA, postdeadline paper: **PD-4**.

[36] Rao, Y.J., *et al.*, 1996. *A novel high-resolution, wavelength-division-multiplexed in-fibre Bragg grating sensor system*. Electron. Lett., Vol. **32**: pp 924-6.

[37] Theriault, S., *et al.*, 1996. *High-g accelerometer based on an in-fibre Bragg grating sensor*. Proc. 11th Int. Conf. on Optical Fibre Sensors, Sapporo, Japan, pp 196-9.

[38] Webb, D.J., *et al.*, 1996. *Miniature fibre optic ultrasonic probe*. Proc. SPIE, Vol. **2839**: paper 8.

[39] Xu, M.G., *et al.*, 1993. *Optical in-fibre grating high pressure sensor*. Electron. Lett., Vol. **29**: pp 398-9.

[40] Yu, F., and Y. Shizhuo, 2002. *Fiber optic sensor*. Marcel Dekker, Inc., USA.

[41] Gholamzadeh, B. and N. Hooman, 2008. *Fiber optic sensors*. World Academy of Science, Engineering and Technology, Vol **42**.

[42] Méndez, A., and T.F. Morse, 2007. *Specialty optical fibers handbook*. Elsevier, USA.

[43] Nogueira, R.N., 2005. *Redes de Bragg em fibra óptica*. Universidade de Aveiro, Dep. Física.

[44] Hill, K.O., *et al.*, 1978. *Photosensivity in optical fiber waveguides: application to reflection filter fabrication*. Appl. Phys. Lett., Vol. **32**: pp 647-649.

[45] Meltz, G., *et al.*, 1989. *Formation of Bragg gratings in optical fibers by a transverse holographic method*. Opt. Lett., Vol. **14**, pp 823-825.

[46] Ghatak, A., and K. Thyagarakan, 2008. *Introduction to fiber optics*. Cambridge University Press, Cambridge, UK.

[47] Kashyap, R., 1999. *Fiber Bragg gratings*. Academic Press, UK.

[48] Rao, Y.J., 1997. *In-fibre Bragg grating sensors*. Meas. Sci. Technol., Vol. **8**: pp 355-375.

[49] Bass, M., and E van Stryland, 2002. *Fiber optics handbook*. McGraw-Hill, Optical Society of America, USA.

[50] Tahir, B.A., *et al.*, 2007. *Review of fabrication techniques of fiber gratings*. Journal of Eng. Appl. Sci., Vol. **2**(1): pp 105-115.

[51] Hill, K.O., *et al.*, 1993. *Bragg gratings fabricated in monomode photosensitive optical fiber by UV exposure through a phase mask*. Appl. Phys. Lett., Vol. **62**: pp 1035-1037.

[52] Anderson, D.Z., *et al.*, 1993. *Production of in fiber gratings using a diffractive optical element*. Elec. Lett., Vol. **29**:pp 566-568.

[53] Hecht, Eugene, 1998. *Óptica*. Fundação Calouste Gulbenkian, Lisboa, Portugal.

[54] Dutton, H.R., 1998. *Understanding optical communications*. IBM International Technical Support Organization, USA.

[55] Malo, B, *et al.*, 1995. *Apodised in-fiber Bragg grating reflectors photoimprinted using a phase mask*. Electron. Lett., Vol. **31**: pp 223-224.

[56] Albert, J., *et al.*, 1995. *Apodisation of the spectral response of fiber Bragg gratings using a phase mask with variable diffraction efficiency*. Electron. Lett., Vol **31**: pp 222-223.

[57] Kersey, A.D., *et al.*, 1997. *Fiber grating sensors*. Journal of Lightwave Technology, Vol. **15**: pp 1442-1463.

[58] Hill, K.O., and G. Meltz, 1997. *Fiber Bragg gratings technology: fundamentals and overview*. OSA/IEEE Journal of Lightwave Technology, Vol. **15**, n. 8: pp 1263-1276.

[59] Xu, M.G., L. Reekie, Y. Chow, and J.P. Daikin, 1993. *Optical in-fiber grating high pressure sensor*, Electron. Lett. **29**, pp 398–9.

[60] Liu Y.,Z. Guo, Y. Zhang, K.S. Chiang, and X. Dong, 2000. *Simultaneous pressure and temperature measurement with polymer-coated fibre Bragg grating*, Electron. Lett., Vol. **36**: pp 564–6.

[61] Zhao Y., C. Yu, and Y. Liao, 2004. *Differential FBG sensor for temperature-compensated high-pressure (or displacement) measurement*, Opt. Laser Technol., Vol. **36**: pp 39–42.

[62] Xu M.G., H. Geiger, and J.P. Daikin, 1996. *Fiber grating pressure sensor with enhanced sensitivity using a glass-bubble housing*, Electron. Lett., Vol. **32**: pp 128–9.

[63] Zhang Y., D. Feng, Z. Liu, Z. Guo, X. Dong, K.S. Chiang, and B.C.B. Chu, 2001. *High-sensitivity pressure sensor using a shielded polymer-coated fiber grating*, IEEE Photon. Technol. Lett., Vol. **13**: pp 618–9.

[64] Zhang W., *et al.*, 2001. *FBG-type sensor for simultaneous measurement of force (or displacement) and temperature based on bilateral cantilever beam*, IEEE Photonics Technol. Lett., Vol. **13**(12): pp 1340–2.

[65] Dong X., B.O. Guan, S. Yuan, X. Dong, and H.Y. Dang, 2002. *Strain gradient chirp of uniform fiber Bragg grating without shift of central Bragg wavelength*, Opt. Commun., Vol. **202**: pp 91–5.

[66] Guan B.O., H.Y. Tam, X.M. Tao, and X.Y. Dong, 2000. *Simultaneous strain and temperature measurement using a superstructure fiber Bragg grating*, IEEE Photonics Technol. Lett., Vol. **12**(6): pp 675–7.

[67] Malucelli, G., 2004. *Polyurethane resin-based adhesives: curing reaction and properties of cured systems*. International

[68] *http://www.ides.com/generics/PUR/PUR_typical_properties.htm*

[69] *http://www.liquid-lens.com*

[70] Alberto, N., *et al.*, 2008. Study of dental gypsum using fibre sensors. BIOSTEC 2008 - International Joint Conference on Biomedical Engineering Systems and Techologies, Vol. **1**: pp 232-235.

[71] Ferreira, L., *et al.*, 2009. *Monitorization of sea sand transport in coastal areas using optical fiber sensors*, article presented at 2009 IEEE Sensors Conference, Christchurch, New Zealand.